8-15-2009

Geologic Setting of the Phoenix Lander Mission Landing Site

Tabatha Heet

Recommended Citation

Heet, Tabatha, "Geologic Setting of the Phoenix Lander Mission Landing Site" (2009). *All Theses and Dissertations (ETDs)*. 931.
https://openscholarship.wustl.edu/etd/931

WASHINGTON UNIVERSITY

Department of Earth and Planetary Sciences

GEOLOGIC SETTING OF THE PHOENIX LANDER MISSION LANDING SITE

by

Tabatha Lynn Heet

A thesis presented to the
Graduate School of Arts and Sciences
of Washington University in
partial fulfillment of the
requirements for the
degree of Master of Arts

August 2009

Saint Louis, Missouri

Acknowledgements

We thank the superb team of Phoenix engineers and scientists for the successful operations of the Lander over the 152 sol period of operations and also the science and engineering teams that provided the orbital image data used in our analyses.

Table of Contents

List of Figures

List of Tables

Abstract

The Phoenix Lander touched down on the northern distal flank of the shield volcano Alba Patera in a ~150 km wide valley underlain by the Scandia Formation. The geomorphology and geology of the landing site is dominated by the ~0.6 Ga, 11.5 km wide, bowl-shaped impact crater, Heimdal, and its areally extensive ejecta deposits. The Lander is located ~20 km to the west of the crater and is sitting on a plains surface underlain by partially eroded Heimdal ejecta deposits. Heimdal was produced by a hypervelocity impact into fine-grained, ice-rich material and is inferred to have produced high velocity winds and a ground-hugging ejecta emplacement mode that destroyed or buried preexisting surfaces and rock fields out to ~10 crater radii. Patterned ground is ubiquitous, with complex polygon patterns and rock rubble piles located on older plains (~3.3 Ga) to the west of the ejecta deposits. Crater size frequency distributions are complex and represent equilibria between crater production and destruction processes (e.g., aeolian infill, cryoturbation, relaxation of icy substrate). Rock abundances increase near craters for the older plains and rocks with their dark shadows explain the reason for the few percent lower albedo for these plains as opposed to the Heimdal ejecta deposits. Many rocks at the landing site have been reworked by cryoturbation and moved to polygon troughs. The evidence for cryoturbation and the lack of aeolian features imply that the soils sampled by Phoenix are locally derived and mixed with a subordinate amount of wind-blown dust.

1. Introduction

The Mars Phoenix Lander touched down in the northern plains of Mars at coordinates 68.22N, 234.25E (areocentric) at an elevation of -4.13km (relative to the MOLA defined areoid [*Zuber et al.* 1992]) on 25 May 2008. Phoenix was the first landed mission to investigate the high northern latitude regions of Mars, touching down ~20 degrees further north than the Viking Lander 2 spacecraft. The primary goals of the Phoenix Mission were to sample and characterize shallow icy soil and the overlying soil deposits and to document the high latitude surface and atmospheric environments [*Smith et al.* 2008].

This paper provides information on the geomorphic and geologic setting of the landing site on regional to local scales using orbital and Phoenix data, with a focus on the influence of emplacement of ejecta deposits from the 11.5 km wide, bowl-shaped impact crater Heimdal, located ~20 km to the east of the landing site. In addition, relative and absolute chronologies are derived from crater distributions for each geologic unit, and deviations from production functions are used to understand processes that alter plains surfaces. Relationships between rock abundances and craters, reworking of local rocks by cryoturbation, and a discussion of the provenance of soils sampled by Phoenix are also covered in this paper.

2. Data Sets and Methodology

Orbital Data Sets: Key to this study was the acquisition and processing of a number of image-based data sets into a co-registered, map-based framework which maintained the spatial resolution inherent to each of the data sets. Key data sets included those acquired from the Mars Reconnaissance Orbiter (MRO) Context Imager (CTX)

[*Malin et al.* 2007], High Resolution Imaging Science Experiment (HiRISE) [*McEwen et al.* 2007] (see Table 1 for specific images used), and CRISM hyperspectral imager [*Murchie et al.* 2007]. Mars Odyssey Thermal Emission Imaging System (THEMIS) [*Christensen et al.* 2004], and Mars Global Surveyor Mars Orbiter Laser Altimeter (MOLA) [*Zuber et al.* 1992] were also included in the analyses. CTX acquires ~30 km wide images at 5-6 m/pixel spatial resolution. The instrument operates in the visible wavelength region with one band covering 0.5-0.7 µm wavelength. HiRISE acquires ~6 km wide images at 0.25-0.32 m/pixel spatial resolution. The instrument operates in the visible wavelengths with three band passes (for color) from 0.54 – 0.87 µm. CRISM data used in the analyses focused on Full Resolution Targeted (FRT) Mode data covering about 10 km in width with 18 m/pixel spatial resolution, and 545 bands from 0.35 to 3.9 µm. THEMIS is a multispectral camera with five wavelengths in the visible (0.425 – 0.860 µm) and ten in the infrared (6.78-14.88 µm). THEMIS acquires data in the visible region at 18 m/pixel and in the infrared at 100 m/pixel spatial resolution. Surface elevation was derived from MOLA 128 pixel/degree (~100 m/pixel) gridded data. Individual MOLA laser pulses were used were increased resolution was required. Individual surface shots cover 130 m on the surface with an absolute vertical accuracy of <10m and a vertical precision of 0.375 m relative to nearby shots.

Orbital Data Processing, Map Generation, and Feature Measurements: The study region extends from 67.5-68.5 N and 231.5-236.5 E in areocentric coordinates and was chosen based on initial prelanding maps generated by *Seelos et al.* [2008]. This region covers the broad valley that Phoenix landed on and surrounding highlands. Imaging data were obtained, processed to map-projected images, and mosaicked to a north polar stereographic projection centered at 233.5 E , with data maintained at full spatial resolution in geophysical units. ArcMap was used to mosaic the data sets, using CTX data as a base, with gaps in coverage filled in using THEMIS visible data. THEMIS daytime thermal IR data were used to fill any remaining gaps. CRISM and HiRISE data were added as additional layers, along with MOLA gridded data. For selected locations, MOLA along track data were also included. CRISM data were processed to Spectral Lambert Albedos for each pixel using DISORT-based retrieval in which dust and ice aerosols, combined with gas bands were explicitly modeled using techniques presented in *Arvidson et al.* [2006].

Generation of the geologic map for the study area was done in a GIS environment by tracing contacts between units and adding them to a database as a set of vector files. Units were defined based on geomorphology, relative albedos, superposition, and embayment relationships. The primary map layer used to generate the units was the CTX mosaic and features as small as 50 m in width were included. Elevation data from gridded MOLA data and individual MOLA profiles were used as needed to clarify geologic relationships and contacts.

Crater sizes and locations were derived from the CTX base map at its full 5 m/pixel resolution by treating sizes and locations as a set of vectors. Likewise rock sizes and locations were also derived and placed in the data base using the higher resolution HiRISE data.

Phoenix Data Sets and Processing: The primary Phoenix data set used in this study was the stereo images generated from the Surface Stereo Imager (SSI) [*Lemmon et al.* 2009]. Rocks within a 5m radius of the lander were located and their widths tabulated using SSI radiometrically-corrected linearized reduced data record images and associated positioning information mosaicked in ArcMap. Areas covered by the rocks were derived from Cartesian coordinate system projections of SSI mosaics, along with delineation of whether the rocks were on patterned ground polygon tops or in intervening troughs.

3. Geologic Mapping

Background: The Phoenix landing site is located in the Borealis basin on the northwest flank of the shield volcano Alba Patera (Fig 1). The northern extent of the Alba Patera Formation is located ~500 km to the south of the landing site and exhibits long lava flows and other evidence of emplacement of volcanic materials from Alba Patera [*Tanaka et al.* 2008]. Phoenix landed on plains located in a NE-SW trending, ~150 km wide, 150 m deep valley mapped by *Tanaka et al.* [2008] as underlain by the Scandia Formation (ABs) (Fig 2). The surrounding uplands surfaces are mapped by these authors as underlain by the Vastitas Borealis Marginal unit (ABvm). The Vastitas Borealis Interior unit (ABvi) is located to the east of the landing site and is a unit that is interpreted to underlie most of the northern plains (Fig 1). The Scandia unit is interpreted to be younger than the Vastitas Borealis units, even though it is often topographically lower [*Seelos et al.* 2008]. *Tanaka et al.* (2008) hypothesize that the Vastitas Borealis Interior unit consists of outflow channel sediments that were deposited as a result of catastrophic discharge characteristic of the late Hesperian epoch. The surface morphology is interpreted to be due to extensive resurfacing caused by mobilization and release of volatiles within the discharge sediments. The history of the Vastitas Borealis Marginal unit is not well understood, but probably represents localized disruption and deformation along the Vastitas Borealis Interior unit margin. *Tanaka et al.* [2008]

hypothesize that a regional thermal anomaly associated with magmatic activity in Alba Patera caused resurfacing of the Vastitas Borealis Interior unit to form the Scandia unit. Possible mechanisms include mud diapirism and volcanism and phreatic or cryoclastic eruptions related to hydrothermal groundwater circulation through fracture systems radial to Alba Patera.

With the background presented in the previous paragraph we define detailed units mapped from the image data bases for the valley and surrounding highlands (Fig. 2).

Crater Interior and Crater Ejecta: Craters and associated ejecta deposits in the valley and surrounding highlands were mapped based on topography and albedo patterns. Pedestal craters, which rise above the surrounding terrain are common in all units. In addition a number of degraded craters were identified that do not have discernable ejecta deposits.

Heimdal: At 11.5 km in diameter, Heimdal is the largest crater in the study area and the crater and associated ejecta deposits dominate the eastern portion of the mapped area (Fig 2). The crater is bowl-shaped and associated lobed ejecta deposits extend up to 30 km radial distance from the crater rim, with evidence of emplacement visible out to ~10 crater radii in some places. The interior of the crater is covered by patterned ground and shows evidence of mass wasting and sublimation pits (fig 4). Ice is visible in the shadows of rocks around the southern rim of the crater (fig 4). We could find no rock outcrops, even on the steep outer walls of the crater.

Heimdal Inner Ejecta: The Inner Ejecta deposits extend from the crater rim radially outward to 2-8 km (azimuthally dependent) and form a moat-like structure that surrounds the crater. These deposits form a broad, low rampart at their distal edges (fig.

5). These deposits are also characterized by >19 rocks larger than 1.5m / hectare (fig. 4) and high (~10°) local slopes relative to Heimdal Outer Ejecta.

Heimdal Outer Ejecta: In THEMIS nighttime Infrared images, Heimdal Outer Ejecta appears as an area of low thermal inertia relative to the surrounding Lowland and Highland Plains. Where intact, its edge is lobate (fig. 6) and characterized by complex patterned ground and 0-3 rocks larger than 1.5 m/ha. The presence of the lobate edge is azimuthally dependent, appearing mainly to the south and north of Heimdal, but not present to the west. To the west, the Outer Ejecta lacks a distinct edge. It is characterized at its terminus by a higher albedo relative to the Lowlands Plains, 0-3 rocks larger than 1.5 m/ha, and ubiquitous ~5m scale polygons. Within the Outer Ejecta, discontinuous deposits rise about 1m above the surrounding terrain as evidenced by shading variations in CTX images (fig. 7). These deposits differ from the non-lobate portion of Heimdal Outer Ejecta in that they are slightly darker due to a network of dark ~20m scale polygon troughs (fig. 7). This same complex patterned ground is also observed on the intact lobate edges. We hypothesize that the difference in morphology within the Outer Ejecta deposit is due to differential erosion of the original ejecta deposit, exposing underlying bright material and leaving topographically higher deposits with preserved ~20m patterned ground and intact lobate edges. The Phoenix lander is located on a small preserved Outer Ejecta deposit ~20km from the crater rim.

Lowland Plains: The Lowland Plains is a subunit of the Scandia Formation consisting of shallow, irregular enclosed basins and is differentiated from the Heimdal Outer Ejecta by a lower albedo and higher rock (>19 rocks >1.5m/ha) and crater abundances (fig 9). Further, rocks are sorted into rubble piles spaced on average ~20m apart. Ubiquitous ~5m polygons are superposed on these rubble piles.

To understand the albedo difference between the Outer Ejecta and Lowland Plains units, representative CRISM spectra were extracted from FRT0003957 for the Outer Ejecta and for shadowed regions within the Outer Ejecta. The two were linearly mixed until they reproduced the Lowland Plains spectrum. The difference in albedo between the Outer Ejecta and the LowlandsPlains can be explained by a 2-3% increased shadow coverage due to the presence of rock rubble piles and associated dark shadows in the Lowland Plains, which are non-existent in the Outer Ejecta deposits.

Knobby Terrain:. This unit consists of rounded, commonly clustered hills (fig. 10). They are identified mainly by topographic expression, rising tens to hundreds of meters above the surrounding terrain. They are 2.5-5 km in basal diameter and exist throughout the region with no obvious relationship to other units. In both HiRISE and CTX images stone stripes are visible along the sloping sides of the knobs. Ubiquitous across the landing site, ~5m polygons are also visible. A lack of craters and aerial extent precluded dating of Knobby Terrain.

*Highland Plains :*This sub-unit of the Vastitas Borealis Marginal unit consists of relatively smooth plains which rise 150-275 m above the Lowland Plains (fig. 2). It is characterized by ubiquitous ~5m wide polygons, few craters, and 9-19 rocks >1.5m/ha.

Blocks and Mesas: This sub-unit of the Vastitas Borealis Marginal unit consists of flat-topped mesas and interlocking blocks 5-50 km in width and raised a few tens of meters above the surrounding Highlands terrain (fig 2). This unit is located mainly at the southern end of the mapped region, but isolated blocks exist to the north which suggests that this unit was once more areally extensive. Total relief from the tops of the mesas to the Lowland Plains is 200-300m. On a small scale the surface is characterized by patterned ground ~5m trough to trough and 9-19 rocks >1.5m/ha.

4. Crater size-frequency Distribution Production and Equilibrium Modeling

Age and Equilibrium Models: Inferences about the ages and degradational histories of geologic units are explored in this section using the crater size frequency distributions. Because only a small portion of the Highlands Plains and the Blocks and Mesas unit are covered in CTX images we did not attempt to analyze crater data for these units, although we were able to determine from crater size-frequency distributions that the Blocks and Mesas unit is older than the Lowland Plains.

There are few craters larger than 1km in the mapped region. Thus to get a statistically significant sample craters as small as ~100m were included in the final distribution. There is some controversy surrounding the use of small (<1km) craters to date planetary surfaces because of a perceived contamination effect by secondary craters [*e.g. McEwen* 2003*; Ivanov* 2001]. We believe our analysis to be valid because we utilize production functions from *Hartmann* [2007] in which secondaries are included in the model as part of the signal, as opposed to the noise [*Hartmann* 2004*; Hartmann* 2007].

Absolute ages were derived by applying the Levenberg-Marquardt algorithm to find the best fit, in a least-squares sense, to a mathematical crater model that incorporates both production and destruction of craters. The Hartmann Production Function [*Hartmann and Neukum* 2001*; Hartmann* 2004] for Mars was used to model the number of craters expected on a surface of a given age assuming no crater destruction. To model crater removal we assume a depth-dependent crater obliteration process [*Phillips and Malin* 1980*; Plaut et al.* 1988], in which craters of a given depth formed before a "critical time" (t*) will be destroyed by subsequent deposition. A crater that is younger than its depth-dependent t* will survive into the present. Crater depth was made equivalent to crater diameter using the depth-diameter relationships for Martian craters derived by *Garvin et al.* [2000].

The differential crater size-frequency distribution can be written as

$$N(D,t^*) = \alpha\{R_p(t_p-t^*)+A\exp[B(t_p-t^*)]\}D^{-(\alpha+1)} \qquad (1)$$

N = differential crater size-frequency distribution

D = crater diameter

R_p = present cratering rate

A,B = parameters describing the decay of early exponential cratering rate

t_p = present time

t* = maximum of (1) time of surface formation and (2) critical time for the given diameter

α = constant defining the production slope

Specific values used for equation parameters are Rp = 3 x 10-13 km-2 year-1, A = 1.8 x 10-12 km-2, B = 6 x 10-9 yr-1, α = 2; consistent with the Hartmann Production Function [*Hartmann and Neukum* 2001*; Hartmann* 2004] and all of which were used by *Phillips and Malin* [1980] and *Plaut et al.* [*1988*]. The first term describes a steady cratering component that has dominated in recent times. The second term accounts for craters formed during the early heavy bombardment phase of the Solar System. In this model crater destruction is a generic crater-depth dependent process, and is presented in this context in terms of deposition, though erosion or a combination of deposition and erosion would produce similar results, as long as crater lifetime is proportional to crater depth.

To decrease computation time and aid in the use of the Levenberg-Marquardt fitting algorithm, deposition was parameterized over the following time intervals: 0.0 - 1.0, 1.0 - 2.0, 2.0 - 3.0, 3.0 - 3.5, 3.5 - 4.0, 4.0 - 4.25, 4.25 - 4.5. Ideally an infinite number of deposition bins would have been used, but trial and error showed that this parameterization provided sufficient resolution to fit the model within the error bars of the observed data. Note that in this model time runs from 0Ga, the beginning of the Solar System, to 4.5Ga, present. To eliminate confusion, the remainder of the text and figures will report age in terms of the standard "years before present".

Age Results: The parameters for the best fit model for each geologic unit are detailed in Table 2 and summarized as follows. Crater counts from Heimdal Inner Ejecta and preserved lobed portions of the Outer Ejecta indicate that the crater is 0.6 Ga, the youngest areally extensive material in the mapped area and the youngest Martian landing site to date. The un-lobed portion of Heimdal Outer Ejecta was fit by a 3.0Ga model curve. The Lowland Plains was fit by a 3.3Ga model curve, corresponding to the beginning of the Amazonian Period. Though our coverage of the Blocks and Mesas and Highlands Plains was not ideal, we believe they are slightly older than the Lowland Plains and when fit by model curves, we obtained an age of 3.5Ga.

Equilibrium Modeling Results: Analysis of crater distributions from craters superposed on Heimdal Inner Ejecta, Hiemdal Outer Ejecta, and the Lowland Plains showed two important trends (fig 11). First, the spatial distribution of craters within the Outer Ejecta is heterogeneous across the surface, with craters more numerous near the

Lowland Plains/Outer Ejecta boundary and less numerous near Heimdal crater. To quantify the gradient in crater abundance, the Outer Ejecta was divided into an inner and an outer annulus. Crater counts from the inner annulus (close to Heimdal) have a cumulative distribution slightly higher than that observed on Heimdal Inner and lobed portion of Outer ejecta. Crater counts from the outer annulus (far from Heimdal) appear equivalent to that of the Lowland Plains. This spatial distribution suggests a distance dependent removal of landforms away from Heimdal. Because the Outer Ejecta crater distribution within the inner annulus looks like Heimdal's, and the crater distribution within the outer annulus is indistinguishable from the Lowland Plains, we hypothesize that the Outer Ejecta represents Lowland Plains material but with landforms removed in a distance dependent process associated with Heimdal impact. Evidence of landforms not removed includes rock-free pedestal craters near the Outer Ejecta terminus and rocky knobs within the Outer Ejecta that were presumably topographically high enough to escape resurfacing during ejecta emplacement (fig. 10). It is also likely that differential erosion has played a part in the removal of craters within the Outer Ejecta.

A second important trend is a roll-over in the cumulative size-frequency curves starting at ~300m observed for all geologic units (including Highlands Plains and Blocks and Mesas units, not shown). One factor that could account for this roll-off is obscuration of fine details is atmospheric haze. In their investigation of contrast reduction over the Viking Lander 2 site, *Kahn et al.* [1986] found that under the highest optical depths observed at the site, 24 pixels were needed to resolve features. This corresponds to ~120m features in CTX data. In addition, we performed HiRISE counts over the Lowland Plains, which should certainly have the necessary resolution, even under observed optical depths, to see craters smaller than 300m, yet the roll-off is still present in the HiRISE counts (fig 11). Based on work by *Kahn et al.* [1986] and HiRISE counts we believe that the roll-off is a real phenomenon and indicates that smaller craters are preferentially being removed from the surface. In addition we see degraded craters indicating that craters are indeed being destroyed.

To explain the roll-off in terms of physical processes we used our depth-dependent crater model to recreate the 300m change in slope under four depositional scenarios: (1) constant deposition starting at 3Ga (2) recent deposition starting 0.25Ga and continuing until present (3) recent deposition starting at 1.0Ga (4) discrete periods of depositional alternating with periods of no depositional activity (fig 12). We found that under the constant deposition scenario we can recreate the change in slope but it moves to slightly larger crater diameters for older surfaces. In addition the change in slope is more gradual than that of the observed data and the curves of different ages converge at small diameters. Recent deposition starting at 0.25Ga fits the observed data the best. The change in slope occurs at the same crater diameters, regardless of surface age, and the curves do not fully converge at small sizes. We can additionally constrain our modeled increase in crater obliteration rates to have occurred after Heimdal emplacement, because the change in slope of the observed Heimdal crater distribution is sharply defined. If obliteration had started before emplacement, this change in slope would be so gradual as to be undetectable, as is the case for the 1Ga surface under the constant deposition scenario. Several discrete periods of crater obliteration can also recreate the change in slope at small diameters, but would likely result in multiple bends in the cumulative frequency plot which are not observed in the data.

Whereas this notional modeling is consistent with the data it is certainly not the complete explanation. For example, we observe degraded craters within the Lowland Plains that only have a preserved crater rim and rock fields (fig 13). If infill were the only process in operation, the rocks would be covered as well as the crater. Since the rocks are exposed there must be other factors involved in crater obliteration. These factors could include cryoturbation, which may work rocks to the surface [*Mellon et al.* 2008] even though deposition is in action. In addition viscous relaxation could work to remove craters of either large or small size preferentially depending on the depth of the ice table.

5. Regional Rock Size Frequency Distributions

Establishing Rock Size-Frequency Distributions: Rock size-frequency distributions were determined using HiRISE data which resulted in a resolvability of rocks as small as ~1.5m. The rock population over the landing site was measured within a 1.5 ha rectangular region of HiRISE image PSP_007853_2485 centered over the lander. Rock size was defined as the shadow width perpendicular to the sun's azimuth [*Golombek et al*. 2008]. The observed distribution flattens to horizontal at rock sizes smaller than ~0.75m due to the resolution limit of the image

To determine rock distributions over large areas of the mapped region we used an automatic rock counting algorithm that calculates rock size by fitting an ellipse to the rock shadow, which the algorithm recognizes as the darkest pixels in an image [*Golombek et al* 2008]. The auto-counting method is parameterized by the number of rocks larger than 1.5 meters/hectare and extrapolations to other rock sizes is accomplished through the use of model curves defined by *Golombek and Rapp* [1997] which are of the form

$$F(D) = ke^{-q(k)D} \qquad (2)$$

where k is the cumulative fractional area covered by rocks and D is the rock diameter. The expression for q(k) was derived by *Golombek and Rapp* [1997] by fitting this family of curves to empirical surface rock counts from the Viking Lander 1 (VL1) and Viking Lander 2 (VL2) sites. Apart from allowing extrapolation from the auto-counting parameter, these model curves are used in landing site hazard assessments [i.e. *Arvidson et al.* 2008; *Golombek et al*. 2008; *Golombek et al*. 2003] and to compare distributions from different areas. In some cases, the resolution of HiRISE was too low (0.62m) for the auto-counting method to be useful. In these cases each image was hand-contoured according to the color scale: green = 0-3, yellow = 4-8, orange = 9-19, red = >19 rocks larger than 1.5m/ha (fig. 14).

Correlation with Craters: An important observation is that rocks and craters are positively correlated (fig. 14, fig. 15). This makes sense because impacts usually produce large ejecta blocks. Two interesting deviations from this pattern occur in the region. First, as discussed above, Heimdal ejecta is characterized by the lowest rock abundance in the region. Second, in the high crater density region at the Lowland Plains/Outer Ejecta boundary, there are relatively few rocks. Possible mechanisms for these two anomalous observations will be discussed in detail in the discussion section below.

Comparison to other sites: Rocks at the surface were counted using a series of SSI images mosaicked and projected into a Cartesian coordinate system. Rock size was defined as the average of the short and long dimension of each rock [*Moore et al.* 1987].

We measured rocks out to a radial distance of ~5m because the digital elevation models were not reliable at the required resolution beyond this radius. Phoenix HiRISE and surface rock distributions were compared with surface and HiRISE counts from VL2 and Mars Exploration Rover Spirit sites. The Phoenix landing site is depleted in rocks of all sizes relative to other areas (fig 16). This result was expected because the Phoenix landing site was chosen based on an expectation of low rock abundance as dictated by landing site safety requirements [*Arvidson et al.* 2008]. Unexpected was the observed, strong deviation from model curves. Since VL2 is closest in latitude and presumably environment to the Phoenix site, one would expect model curves based on VL2 counts to match fairly closely the rock distribution at the Phoenix site. In fact, with a much steeper slope than predicted by the model curves, the Phoenix site looks more like the Spirit landing site at Gusev Crater. This same steep slope is observed also at the Mars Pathfinder site and several earth analogue sites [*Golombek and Rapp* 1997; *Golombek et al*. 2008]. Such a strong deviation suggests that a simple crushing law based on fracture and fragmentation theory used to derive the model curves, does not fully explain rock popluations at the Phoenix and other sites. Additionally, it implies that a similar process may be in effect at both the Phoenix and Spirit sites.

6. Local Redistribution of Rocks by Cryoturbation Processes

Surface Morphology and Statistics: Surface rock counts derived from SSI data were divided into units based on the morphology of patterned ground at the landing site [see also *Mellon et al.* 2009], which is characterized by sub-hexagonal polygons with edges lower in elevation than centers. For the purposes of this study, we defined the polygon interior as the raised central portion of the polygon and the polygon trough unit as the depressed edge, with the boundary at the halfway point in elevation between the top of the polygon center and the bottom of the trough. Additionally we calculated average nearest neighbor statistics for rocks larger than 5cm within each unit and for the landing site as a whole. The average nearest neighbor distance describes how clustered/uniformly dispersed the rocks are and is defined as the average distance between each rock's center and its closest neighbor's center. It is reported as the ratio of the average nearest neighbor distance to the average distance for a hypothetical random distribution containing the same number of rocks over the same area [*Ward et al.* 2005]. If the statistic is less than 1, rocks tend to be clustered, whereas greater than 1 indicates they are dispersed. A percentage is given to indicate the level of confidence in the statistic. For example, a confidence level of 0.05 indicates there is a 5% chance that the observed statistic resulted from random chance during sampling and is not a real phenomenon.

Rock Distribution within Polygons: Visually there is a sense that rocks tend to concentrate in polygon troughs (fig 17), though it is certainly not obvious everywhere in the landing site. We calculated the size-frequency distribution for rocks within Polygon Interior and Polygon Trough units (fig 18). There is a slight indication, based on cumulative frequency plots (fig 18), that rocks are indeed sorted into polygon troughs. A chi-squared goodness-of-fit test, testing the null hypothesis that polygon Interior and polygon trough rocks come from the same distribution, was performed on the differential number of rocks binned so that each bin contained 10% of the data. The resulting p-value was 1.2e-5, indicating that it is very unlikely, even though the curves look similar in the cumulative frequency plots, that the differences are due only to sampling errors. In addition, nearest neighbor statistics for rocks larger than 5cm (Table 3) indicate that rocks in troughs tend to be uniformly dispersed, while rocks within polygon interiors tend to be clustered. Rock sorting between polygon units is consistent with thermal-contraction based ice- or sand-wedge polygon formation. This type of patterned ground is formed as winter cooling of the ground causes contraction, which can lead to a honeycomb network of cracks within the surface [*Mellon et al.* 2008]. Material such as ice-melt and wind-blown dust can fall into the crack forming a wedge. Subsequent summer time thermal expansion will result in uplift of the central regions of the polygon as the wedge prevents the surface from reassuming its original extent. Thousands of years of polygon development and wedge growth can lead to tens of cm of relief. The relief and slight lateral movement toward troughs created by incremental uplift of polygon centers causes rocks to shift toward polygon troughs, where, over thousands of years, rocks will become increasingly concentrated.

7. Discussion

Heimdal Emplacement Mechanism: The Heimdal impact was responsible for alteration of the preexisting Scandia Formation plains up to 10 crater radii from the center of the impact. Preexisting landforms were destroyed close to the impact site and rocks and older patterned ground were removed for a larger distance from the impact.

Other craters on Mars, called Double-Layered ejecta (DLE) craters, also lack secondary craters, implying also a lack of large ejecta blocks [*Boyce et al.* 2006], and are observed in THEMIS nighttime IR images in the region surrounding the landing site as ejecta deposits with low thermal inertia values. DLE craters are characterized by two ejecta layers (an inner layer that extends 1-2 radii ending in a broad rampart and an outer layer that extends 3-6 radii thickening toward the perimeter), radial texture, lack of secondary craters, and few large rocks [*Boyce et al.* 2006], all characteristics which are observed for Heimdal. DLE craters are part of a family of craters emplaced by ground-hugging fluidized flow, including Single-layer ejecta (SLE) and Multi-layered ejecta (MLE) craters, but some unique emplacement process not active in the production of these other fluidized ejecta craters created the characteristic two layers as well as the lack of secondary craters and large rocks. *Boyce and Mouginis-Mark* [2006] suggest that wind vortices generated by the advancing ejecta curtain explains the morphology of DLE craters. *Wrobel et al*. [2006] has modeled impact under high atmospheric pressure (0.4 bar) and found that it produces wind vortices with speeds in excess of 200m/s which cause intense erosion of fine-grained ejecta, creating the characteristic moat structure of the inner layer. *Vickery et al.* [1986] models show that ejecta blocks are entrained in the advancing ejecta curtain and high wind-speeds create dynamic pressures on the order of 0.67-29 GPa that are capable of crushing rocks into small fragments. *Wrobel et al.* [2006] has modeled that an impact creating a 10km crater sustained temperatures hot enough to vaporize subsurface ice down to several cm, which would produce a transient, dense gas cloud, increasing the ability of the ejecta curtain to crush rocks. This effect is also enhanced if water is present in the target material as it weakens the ejecta blocks, making them easier to fragment [*Wohletz et al.* 1983]. Emplacement of a fine-grained ejecta layer, thinning outward would entrain and bury rocks, even beyond the radius over which high wind speeds and rock-crushing dynamic pressure are in effect. This mechanism accounts for the distinct lack of rocks within the Heimdal Outer Ejecta ejecta.

It also explains why larger, pre-existing landforms, such as pedestal craters and knobs are preserved at a greater distance from Heimdal, even where rocks have been removed.

Relationship of Observations to Local Geology: The Phoenix lander is located on the distal deposit of preserved Heimdal ejecta ~20km from the crater rim, making the Phoenix landing site the youngest on Mars. These ejecta deposits appear to have been differentially eroded by wind, and they exhibit two scales of polygons, ~5m and ~20m. Evidence of ~20m polygons is also observed as rubble piles spaced ~20m apart in the Lowland Plains. As observed from the surface, polygons tend to sort rocks into troughs, so these rubble piles are likely remnant polygon troughs from the same climate period that created the 20m polygons observed on Heimdal ejecta. Since the sorted rocks are so large, we infer that the previous climate was not short in duration and the major process acting on the Lowland Plains at least in recent times has been cryoturbation.

The regolith at the landing site is 5-15+ cm deep covering water-ice-cemented regolith [*Arvidson et al.* 2009]. The surface soils display cohesion as evidenced by the cloddy nature of excavated trenches [*Arvidson et al.* 2009]. Optical Microscope images show a dominant silt-sand sized matrix, with a less abundant clay-sized component [*Pike et al.* 2009]. The sand grains are typically rounded, indicating transport as part of the saltation load. It is also notable that there are no aeolian deposits or features observed at the landing site. Because of the lack of aeolian features and because of the provenance of cryoturbation features and patterned ground, the main soil transport mechanism appears to be vertical and associated with polygon formation. Thus most soil is likely local is origin, with a subordinate fraction of windblown material

References Cited

Arvidson, R. E., F. Poulet, R. Morris, J.-P. Bibring, J. Bell III, S. Squyres, P. Christensen, G. Bellucci, B. Gondet, B. Ehlmann, W. Farrand, R. Fergason, M. Golombek, J. Griffes, J. Grotzinger, E. Guinness, K. Herkenhoff, J. Johnson, G. Klingelhofer, Y. Langevin, D. Ming, K. Seelos, R. Sullivan, J. Ward, S. Wiseman, M. Wolff (2006) Nature and Origin of the Hematite-Bearing Plains of Terra Meridiani Based on Analysis of Orbital and Mars Exploration Rover Data Sets, J. Geophys. Res., 111, E12S08 doi: 10.1029/2006JE002728.

Arvidson R.E., D. Adams, G. Bonfiglio, P. Christensen, S. Cull, M. Golombek, J. Guinn, E. Guinness, T. Heet, R. Kirk, A. Knudson, M. Malin, M. Mellon, A. McEwen, A. Mushkin, T. Parker, F. Seelos IV, K. Seelos, P. Smith, D. Spencer, T. Stein, L. Tamppari (2008), Mars Exploration Program 2007 Phoenix Landing Site Selection and Characteristics, J. Geophys. Res., 113, E00A03, doi:10.1029/2007JE003021

Arvidson, R., R. Bonitz, M. Robinson, J. Carsten, M. Mellon, P. Chu, K. Davis, J. Wilson, A. Shaw, R. Greenberger, K. Siebach, T. Stein, S. Cull, W. Goetz, R. Morris, D. Ming, H. Keller, M. Lemmon, H. Sizemore, M. Mehta. (2009) Results from the Mars Phoenix Lander Robotic Arm Experiment, submitted in current issue.

Christensen, P. B. Jakosky, H. Keiffer, M. Malin, H. McSween, K. Nealson, G. Mehall, S. Silverman, S. Ferry, M. Caplinger, and M. Ravine (2004), The Thermal Emission Imaging System (THEMIS) for the Mars 2001 Odyssey Mission, Space Sci. Rev., 110, 85-130.

Boyce, J.M and P.J. Mouginis-Mark (2006) Martian craters viewed by the Thermal Emission Imaging System instrument: Double-layered ejecta craters, *J. Geophys. Res.,111, E10005, doi:10.1029/2005JE002638.*

Garvin, J.B., S.E. Sakimoto, J.J. Frawley, C. Schnetzler (2000). North Polar Region Craterforms on mars: Geometric Characteristics from the Mars Orbiter Laser Altimeter. Icarus, v144, pp329-352.

Golombek, M. and D. Rapp (1997), Size-frequency distributions of rocks on Mars and Earth analog sites: Implications for future landed missions, *J. Geophys. Res, 102(E2), p. 4117-4129*.

Golombek, M. P., N. Forsberg-Taylor, E. DiMaggio, R. Schroeder, B. Jakosky, M. Mellon, J. Matijevic, 2003, Rock size-frequency distributions on Mars and implications for MER landing safety and operations: *J. Geophys. Res., v. 108(E12), 8086, doi:10.1029/2002JE002035, 23pp.*

Golombek, M.P., A. Huertas, J. Marlow, B. McGrane, C. Klein, M. Martinez, R.E. Arvidson, T. Heet, L. Barry, K. Seelos, D. Adams, W. Li, J.R. matijevic, T. Parker, H.G. Sizemore, M. Mellon, A.S. McEwen, L.K. Temppari, and Y. Cheng (2008), Size-frequency distributions of rocks on the northern plains of Mars with special reference to Phoenix landing surfaces, submitted to *J. Geopys. Res*.

Hartmann, W.K. and Neukum, G. (2001). Cratering Chronology and the Evolution of Mars, *Space Science Reviews, 96: 165-194.*

Hartmann, W.K. (2004) Marian Cratering 8: Isochron refinement and the chronology of Mars, *Icarus, 174, 294-320, doi: 10.1016/j.icarus.2004.11.023*

Hartmann, W.K. (2007) Martian Cratering 9: Toward resolution of the controversy about small craters, *Icarus, 189, 274-278, doi: 10.1016/j.icarus.2007.02.011*

Ivanov, B. (2001). Mars/Moon cratering rate ratio estimates. In: Kallenbach, R., Geiss, J., Hartmann W.K. (Eds.), Chronology and Evolution of Mars, International Space Science Institute, Bern, 87-104.

Kahn, R., E.A. Guinness, and R.E. Arvidson, 1986, Loss of fine-scale surface texture in Viking Orbiter images due to atmospheric obscuration and a reassessment of latitudinal debris mantling on Mars, *Icarus, 66, 22-38.*

Lemmon, M. et al. (2009) - submitted in current issue

Malin, M., J. Bell, B. Cantor, M. Caplinger, W. Calvin, R. Clancy, K. Edgett, L. Edwards, R. Haberle, P. James, S. Lee, M. Ravine, P. Thomas, M. Wolff (2007) Context Camera Investigation on board the Mars Reconaissance Orbiter, *J. Geophys. Res, 112, E05204, doi:10.1029/2006JE002808.*

McEwen, A.S. (2003) . Secondary crtering on Mars: implications for age dating and surface properties. In: Mars Polar Ice Conference 3rd, Lake Louise, Canada, Oct. 2003, Abstract 3268.

McEwen, A.S., E.M. Eliason, J.W. Begstrom, N. T. Bridges, C.J. Hansen, W. A. Delamere, J. A. Greant, V. C. Gulick, K.E. Herkenhoff, L. Keszthelyi, R. L. Kirk, M.T. Mellon, S.W. Squyres, N. Thomas, and C.M. Weistz (2007) Mars Reconnaissance Orbiter's High Resolution Imaging Science Experiment (HiRISE), *J. Geophys. Res. 112*, E05S02, doi: 10.1029/2005JE002605.

Moore, H.J., R.E. Hutton, G.D. Clow, and C.R. Spitzer (1987). Physical Properties of the Surface Materials at the Viking Landing Sites on Mars, *U.S. Geological Survey Professional Paper 1389, United States Government Printing Office, Washington.*

Murchie S., R.E. Arvidson, P. Bedini, K. Keisser, J.-P. Bibring, J. Bishop, J. Boldt, P. Cavender, T. Choo, R.T. Clancy, E.H. Darlington, D. Des Marais, R. Espiritu, D. Fort, R. Green, E. Guinness, J. Hayes, C. Hash, K. Heffernan, J. Hemmler, G. Heyler, D. Humm, J. Hutcheson, N. Izenberg, R. Lee, J. Lees, D. Lohr, E. Malaret, T. Martin, J.A. McGovern, P. McGuire, R. Morris, J. Mustard, S. Pelkey, E. Rhodes, M. Robinson, T. Roush, E. Schaefer, G. Seagrave, F. Seelos, P. Silverglate, S. Slavney, M. Smith, W.-J. Shyong, K. Strohbehn, H. Taylor, P. Thompson, B. Tossman, M. Wirzburger, and M. Wolff (2007), Compact Reconnaissance Imaging Spectrometer for Mars (CRISM) on Mars Reconnaissance Orbiter (MRO), *J. Geophys. Res., 112*, E05S03, doi:10.1029/2006JE002682.

Mellon, M T., R. E. Arvidson, J Marlow, R. Phillips and E. Asphaug, 2008, Periglacial Landforms at the Phoenix Landing Site and the Northern Plains of Mars, J. Geophys. Res., 113, E00A23, doi:10.1029/2007JE003039.

Mellon, M.T. et al. (2009) - submitted in current issue

Phillips, R.J., M.C. Malin (1980), Ganymede: A Relationship Between Thermal History and Crater Statistics, *Science, 210, 10, 185-188.*

Pike, T. et al. (2009) - submitted in current issue

Plaut, J.J., R. Kahn, E.A. Guinness, R.E. Arvidson (1988). Accumulation of Sedimentary Debris in the South Polar Region of Mars and Implications for Climate History, *Icarus, 76, 357-377.*

Seelos, K. D., F. P. Seelos, R. E. Arvidson, S. Cull, S. L. Murchie, P. McGuire, and T. J. Parker (2008) Geomorphologic and Mineralogic Characterization of the Northern Plains of Mars at the 2007 Phoenix Mission Candidate Landing Sites, *J. Geophys. Res*., X, X

Smith, P., L. Tamppari, R. Arvidson, D. Bass, D. Blaney, W. Boynton, A. Carswell, D. Catling, B. Clark, T. Duck, E. DeJong, D. Fisher, W. Goetz, P. Gunnlaugsson, M. Hecht, V. Hipkin, J. Hoffman, S. Hviid, H. Keller, S. Kounaves, C. Lange, M. Lemmon, M. Madsen, W. Markiewicz, J. Marshall, C. McKay, M. Mellon, D. Michelangeli, D. Ming, R. Morris, N. Renno, W. Pike, U. Staufer, C. Stoker, P. Taylor, J. Whiteway, S. Young, and A. Zent (2008), Introduction to special section on the Phoenix Mission: Landing Site Characterization Experiments, Mission Overviews, and Expected Science, *J. Geophys. Res, 113, doi:10.1029/2008JE003038.*

Tanaka K.L., J.A.P. Rodriguez, J. A. Skinner, M.C. Bourke, C.M. Fortezzo, K.E. Herkenhoff, E.J. Kolb, C.H. Okubo (2008), North polar region of Mars: Advances in stratigraphy, structure, and erosional modification, *Icarus, 196, 318-358.*

Tanaka, K.L., Skinner, and T.M. Hare (2005), Geologic Map of the Northern Plains of Mars, *U.S. Geologic Survey Scientific Investigations Map 2888*.

Vickery, A. (1986) Effect of an Impact-Generated Gas Cloud on the Acceleration of Solid Ejecta, *J. Geophys. Res., 91, B14: 14139-14160.*

Ward, J. G., R. E. Arvidson, and M. Golombek (2005), The size-frequency and areal distribution of rock clasts at the Spirit landing site, Gusev Crater, Mars, Geophys. Res. Lett., 32, L11203, doi:10.1029/2005GL022705.

Wohletz, K.H. and M.F. Sheridan (1983) Martian Rampart Crater Ejecta: Experiments and analysis of melt-water interaction, *Icarus, 56, 15-37*.

Wrobel, K., P. Schultz, D. Crawford (2006) An atmospheric blast/thermal model for the formation of high latitude pedestal craters, *Meteoritics and Planetary Science 41, Nr 10, 1539-1550.*

Zuber M.T., D. E. Smith, S.C. Solomon, D.O. Muhleman, J.W. Head, J.B. Garvin, J.B. Abshire, and J.L. Bufton (1992) The Mars Observer Laser Altimeter Investigation. *J. Geophys. Res., 97, E5, 7781-7797.*

Figures

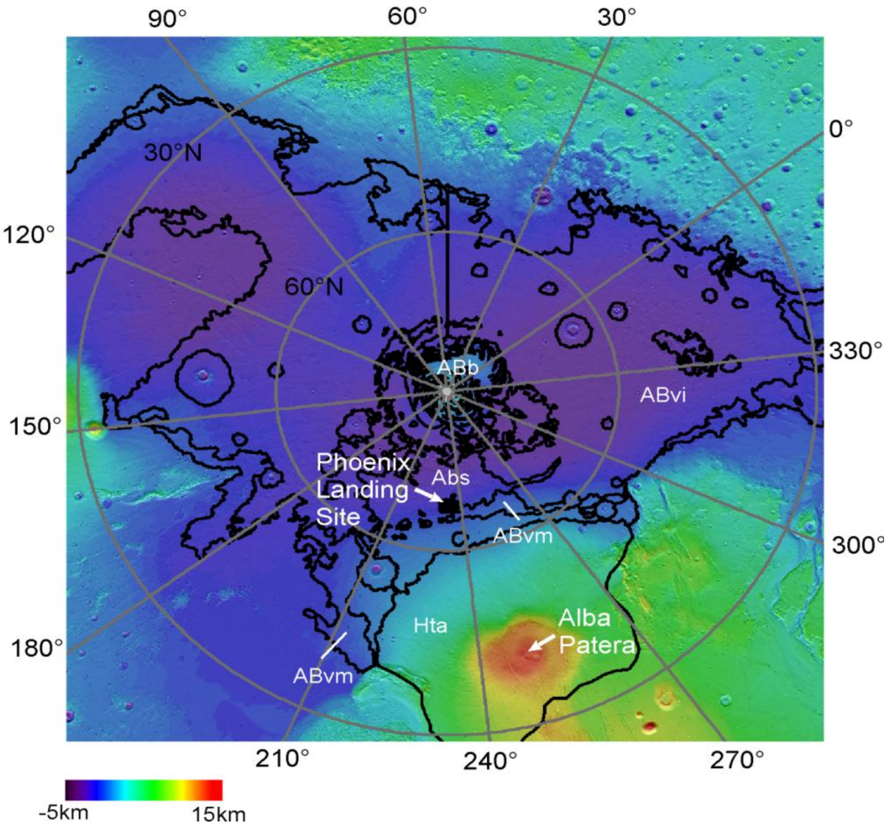

Figure 1. Polar Stereographic map showing MOLA elevation over a shaded relief map. The Phoenix landing site is situated between Planum Boreum (ABb) to the north and Alba Patera to the south. Resurfacing from Alba Patera is visible as little as 500km from the landing site (Alba Patera Formation (Hta) [Tanaka et al. 2005]. On a more local scale Phoenix is located on the Scandia Formation (ABs), near the boundary with the Vastitas Borealis Marginal unit (ABvm). To the east the Vastitas Borealis Marginal unit is gradational with the Vastitas Borealis Interior unit (ABvi) which covers much of the northern plains. Geologic units are based on work by Tanaka et al. [2005] and elevations are relative to the MOLA defined aeroid [Zuber et al. 1992].

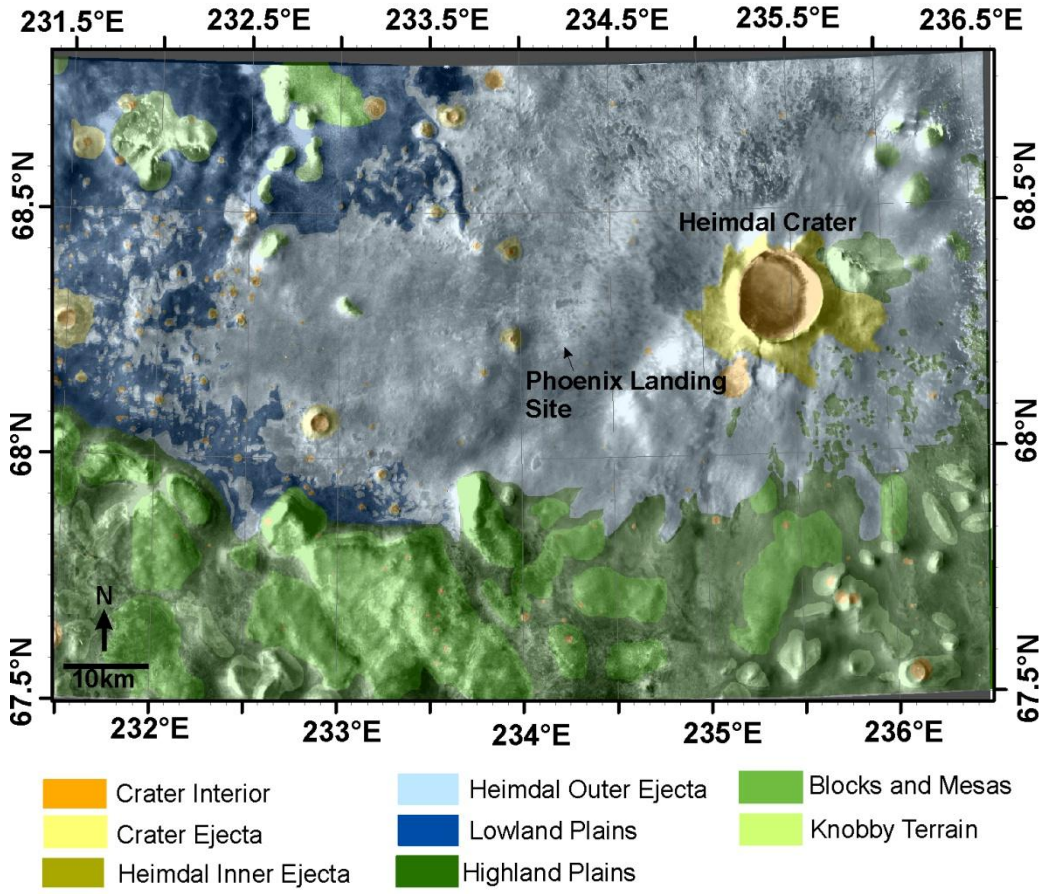

Figure 2. Polar Stereographic map showing detailed geologic units over the Phoenix landing site. The Highland plains and Blocks and Mesas unit correlate spatially with the Vastitas Borealis Marginal unit, whereas the Lowland Plains and Heimdal Outer Ejecta together correlate with the Scandia Formation (see fig. 1). The Blocks and Mesas units consist of flat-topped, usually interlocking blocks rising tens of meters above the intervening Highland plains. These two units are recognized as topographic highs, rising several hundred meters above the valley material. The Lowland Plains and Heimdal Outer Ejecta are plains units that exhibit few geomorphic differences. The Lowland Plains unit has lower albedo, a greater abundance of degraded craters, and extensive rock piles that are missing in the Heimdal Outer Ejecta deposits due to surficial modification by the impact associated a 10km wide, relatively fresh, bowl-shaped impact crater

named Heimdal, whose ejecta deposits dominate the eastern portion of the region. The Phoenix lander is located on a small differentially eroded ejecta deposit ~20km from the crater rim.

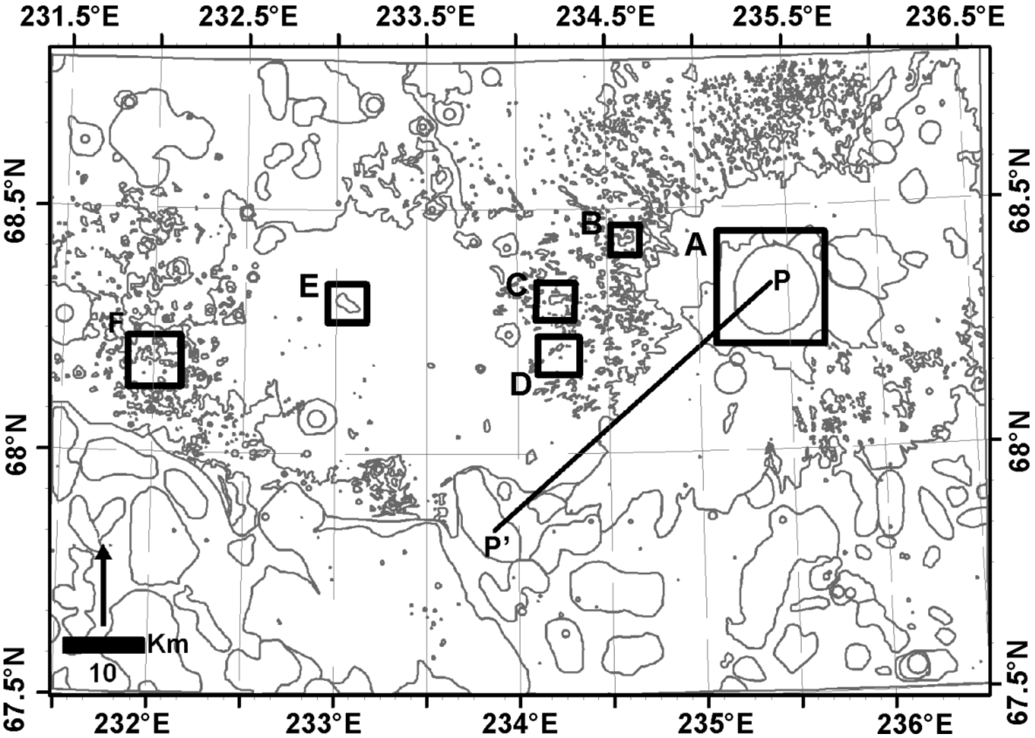

Figure 3. Polar Stereographic map showing outlines of geologic units over the landing site. Black boxes (labeled A, B, C, D, E) indicate locations associated with figures 4 and 6-10.

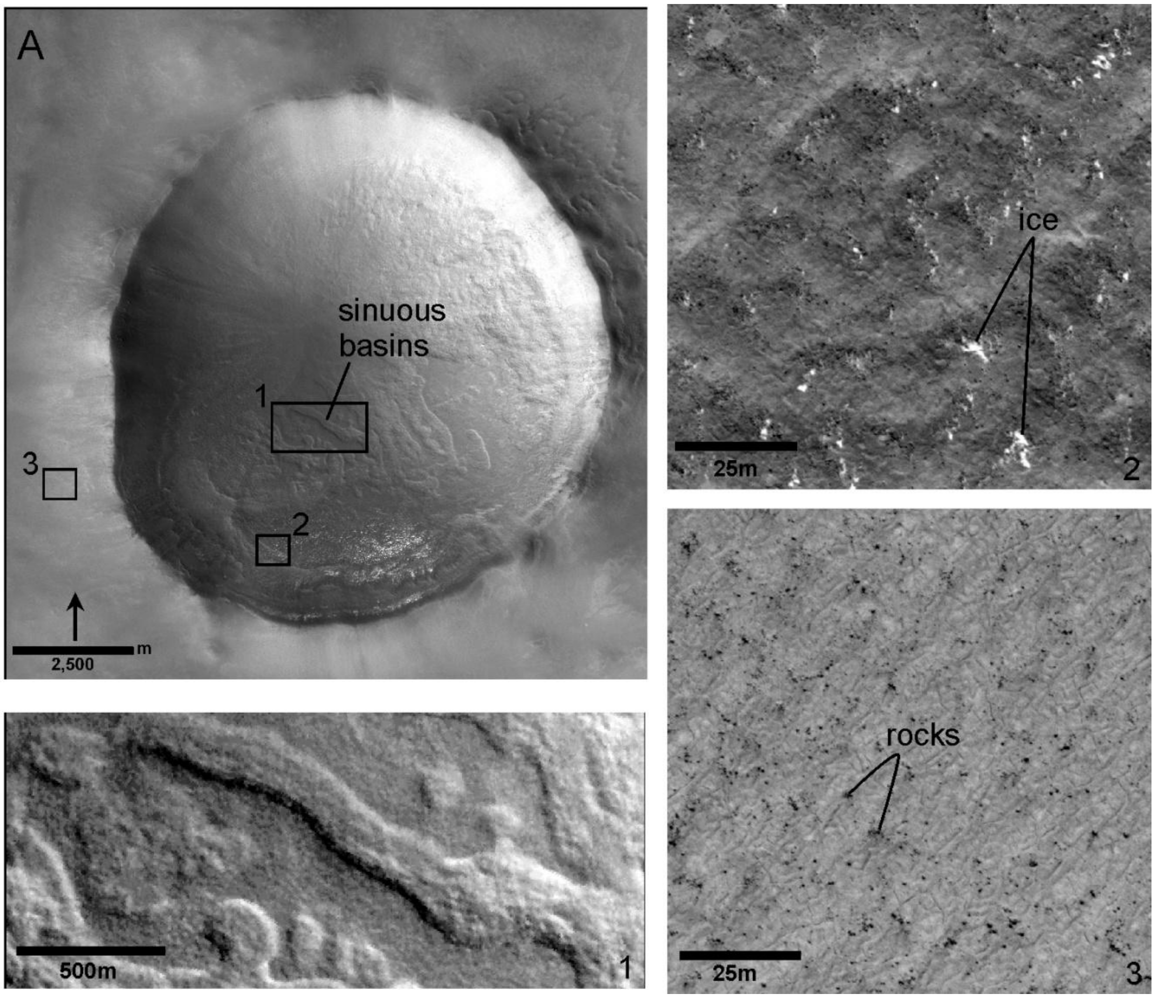

Figure 4. Portion of CTX image P22_009580_2485_XI_68N124W over Heimdal Crater Interior and its Inner Ejecta. (1) Sinuous basins on the crater floor indicate sublimation losses. (2) Permanent water-ice, located mainly in the shadows of large boulders, is visible on the southern rim as high albedo features. (3) surrounding the crater interior is the Heimdal Inner Ejecta, which is characterized by high rock abundance (>19 rocks larger than 1.5m/hectare) and high local slopes (5-10 degrees) relative to the outer ejecta unit. Note also, the ubiquitous patterned ground at ~5m scale.

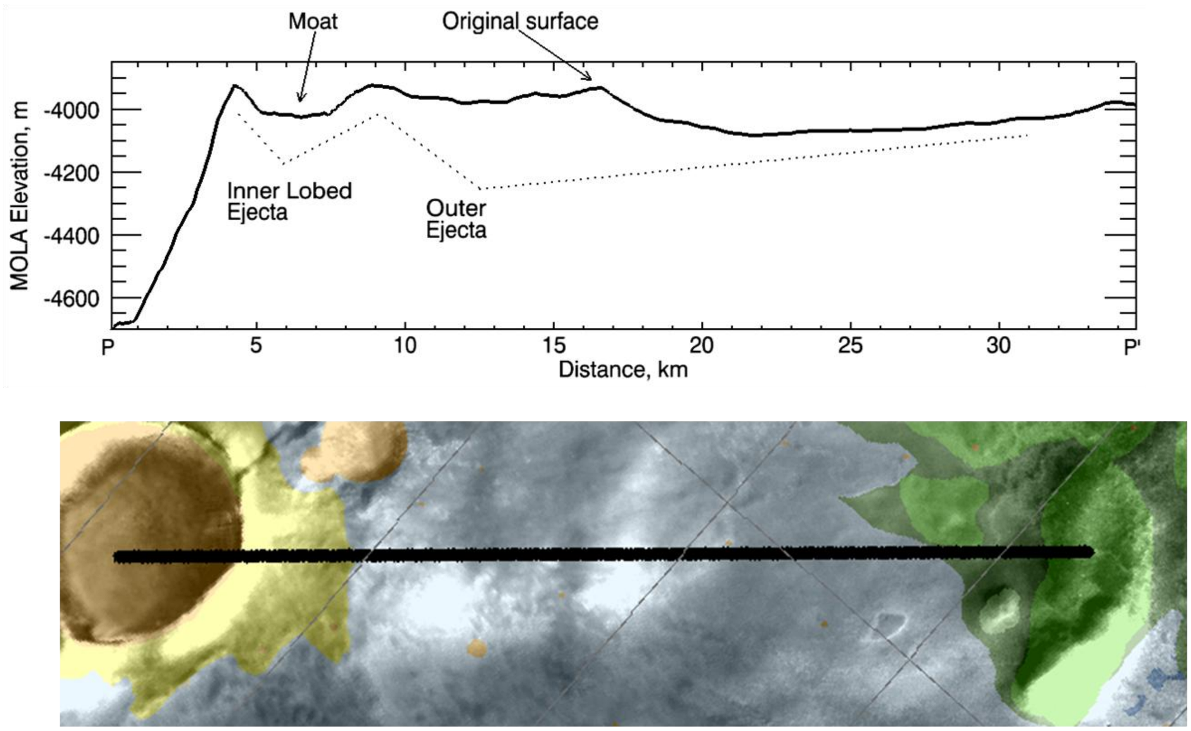

Figure 5. Vertical profile of Heimdal ejecta derived from MOLA 100m gridded data (vertical exageration = 12.5). Two distinct layers of ejecta are observed. The inner layer extends out to about 5km from the crater rim and displays a moat-like morphology ending in a low, broad rampart. The outer layers extends to >30km beyond the crater rim and has been differentially eroded, leaving raised preserved deposits above a higher albedo terrain. Where intact, the original edge of the Outer layer ends in a broad, low rampart, and the morphology is consistent with Double Layered Ejecta type crater.

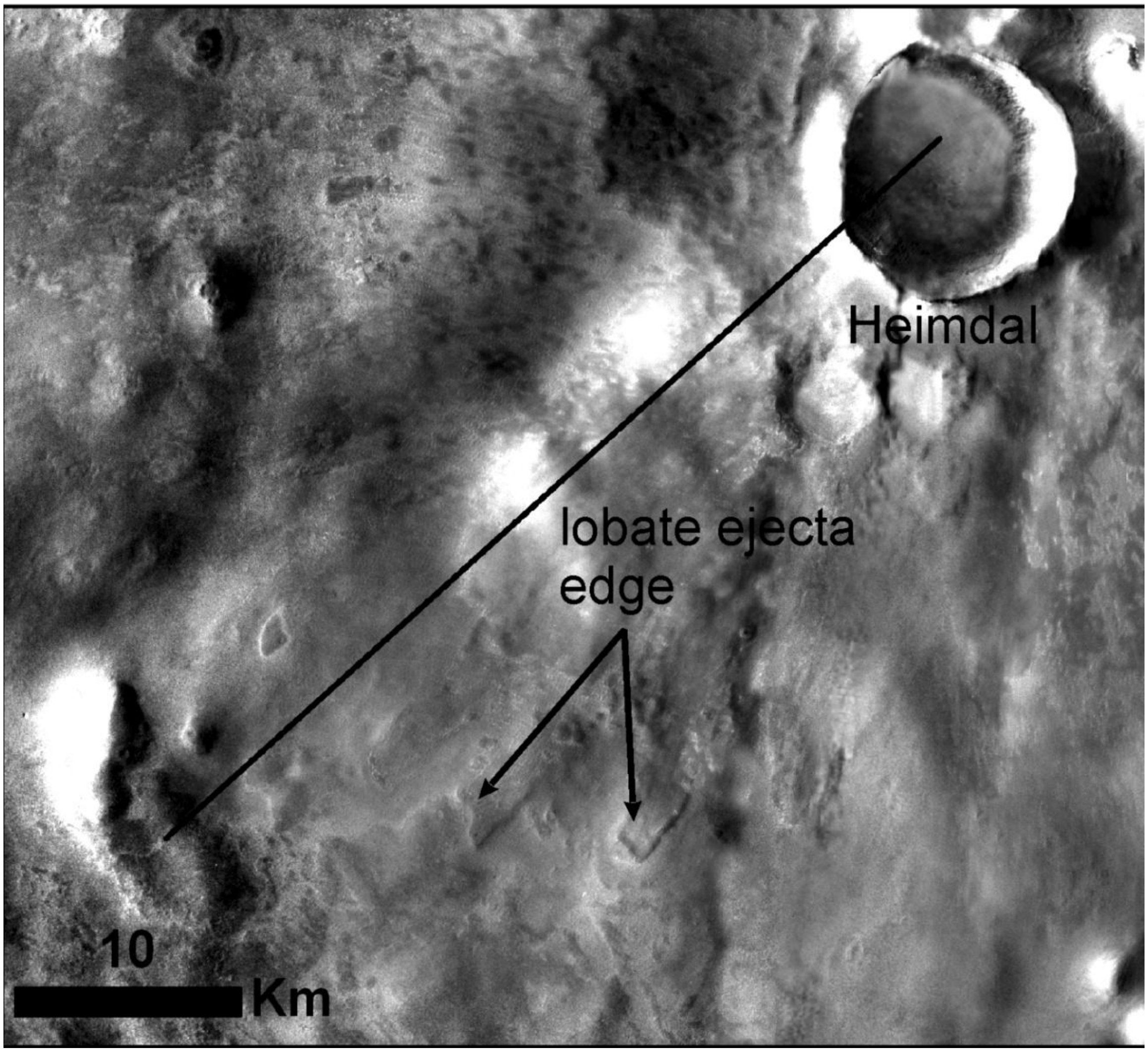

Figure 6. THEMIS visible mosaic showing lobate properties of Heimdal ejecta. Lobate ejecta indicate fluidized ejecta emplacement. Solid line represents location of vertical profile, figure 4.

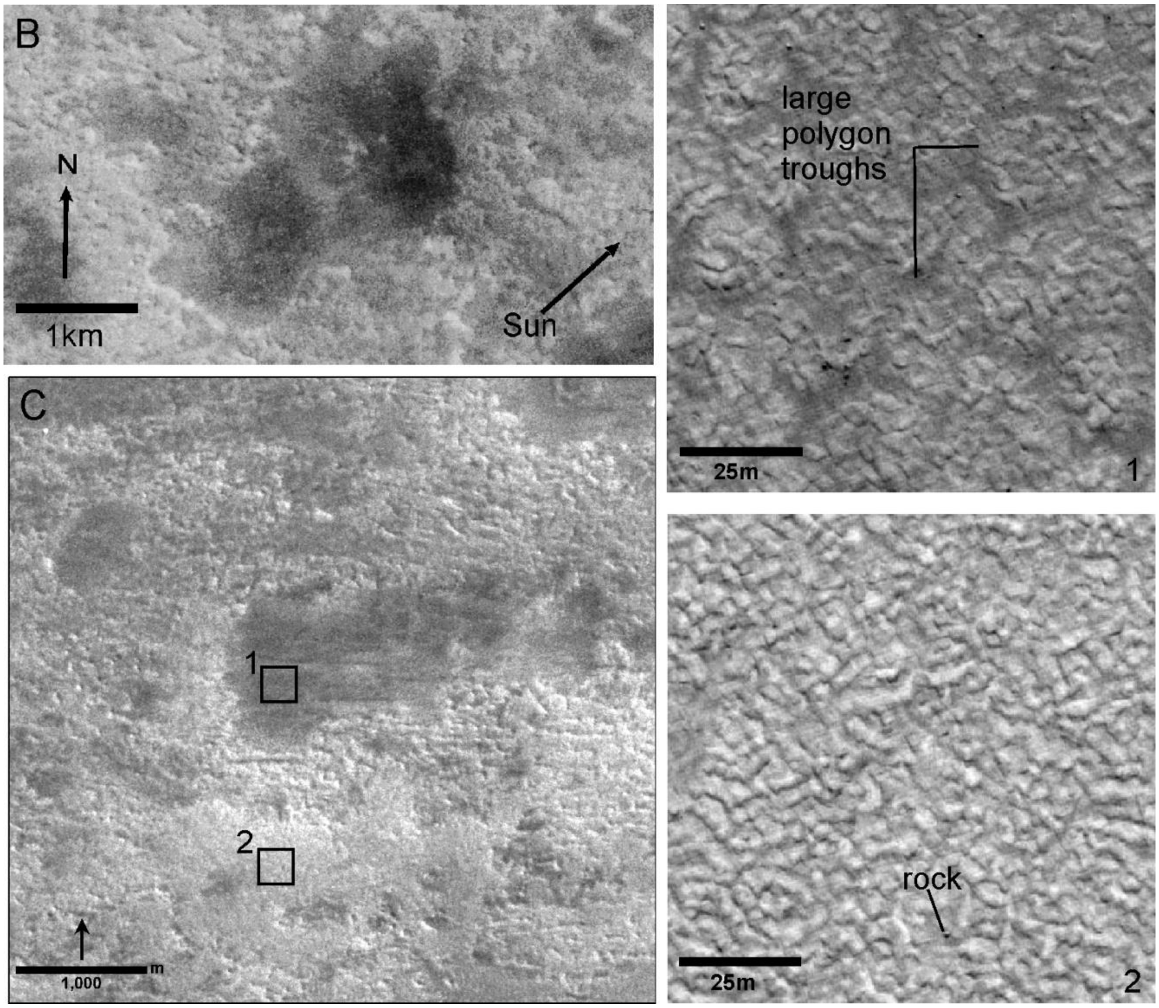

Figure 7. (B) Portion of CTX image P22_009725_2484_XI_68N125W showing differentially eroded Heimdal Outer Ejecta. Shadow pattern indicates that the deposit rises ~1m above the surrounding Heimdal Outer Ejecta. (C) A different portion of the same CTX image showing relatively dark, preserved portion Heimdal Outer Ejecta, surrounded by ligher-toned ejecta material. (1) The dark appearance is due to ~20m scale dark polygon troughs suporposed by smaller ~5m wide polygons. (2) The surrounding Heimdal Outer Ejecta has very few rocks and ubiquitous ~5m scale patterned ground.

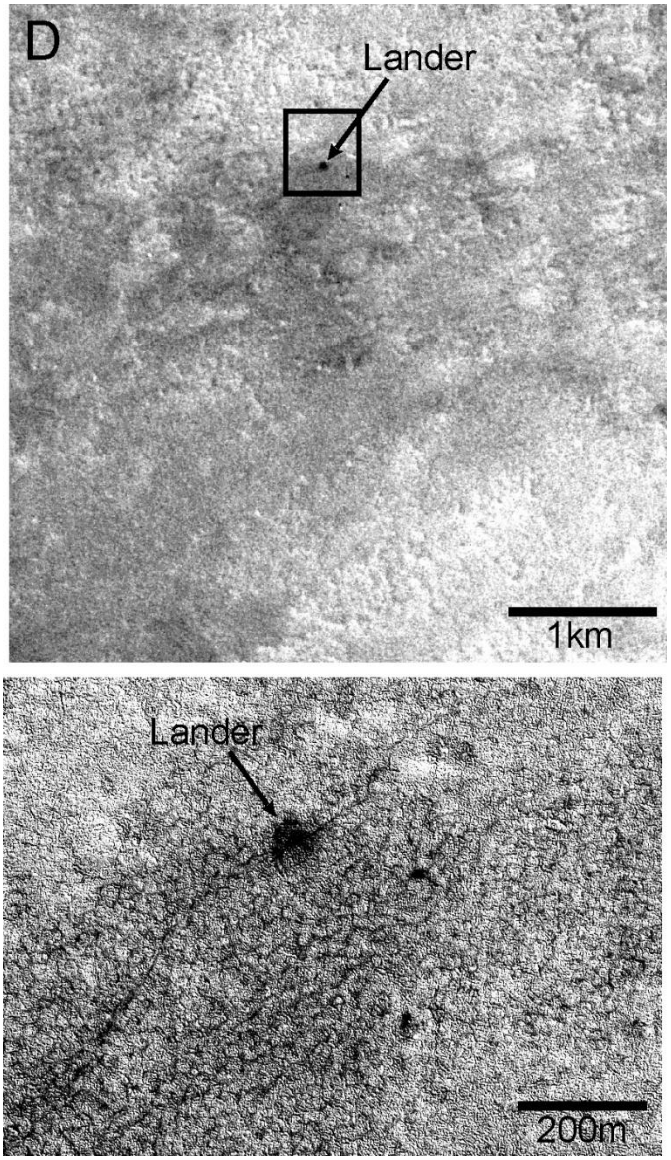

Figure 8. (top) Portion of CTX image P22_009725_2484_XI_68N125W showing the phoenix landing site with the lander location labeled. The lander is located on a dark, differentially eroded Hiemdal Outer Ejecta deposit ~20km west of the crater rim. The surrounding terrain is lighter-toned Heimdal Outer Ejecta which lacks the complex patterned ground of perserved deposits. (bottom) Portion of HiRISE image PSP_009725_2484, showing another view of the dark Heimdal Outer Ejecta deposit. Dark polygon troughs accounting for the dark appearance in CTX and spaced ~20m apart are visible.

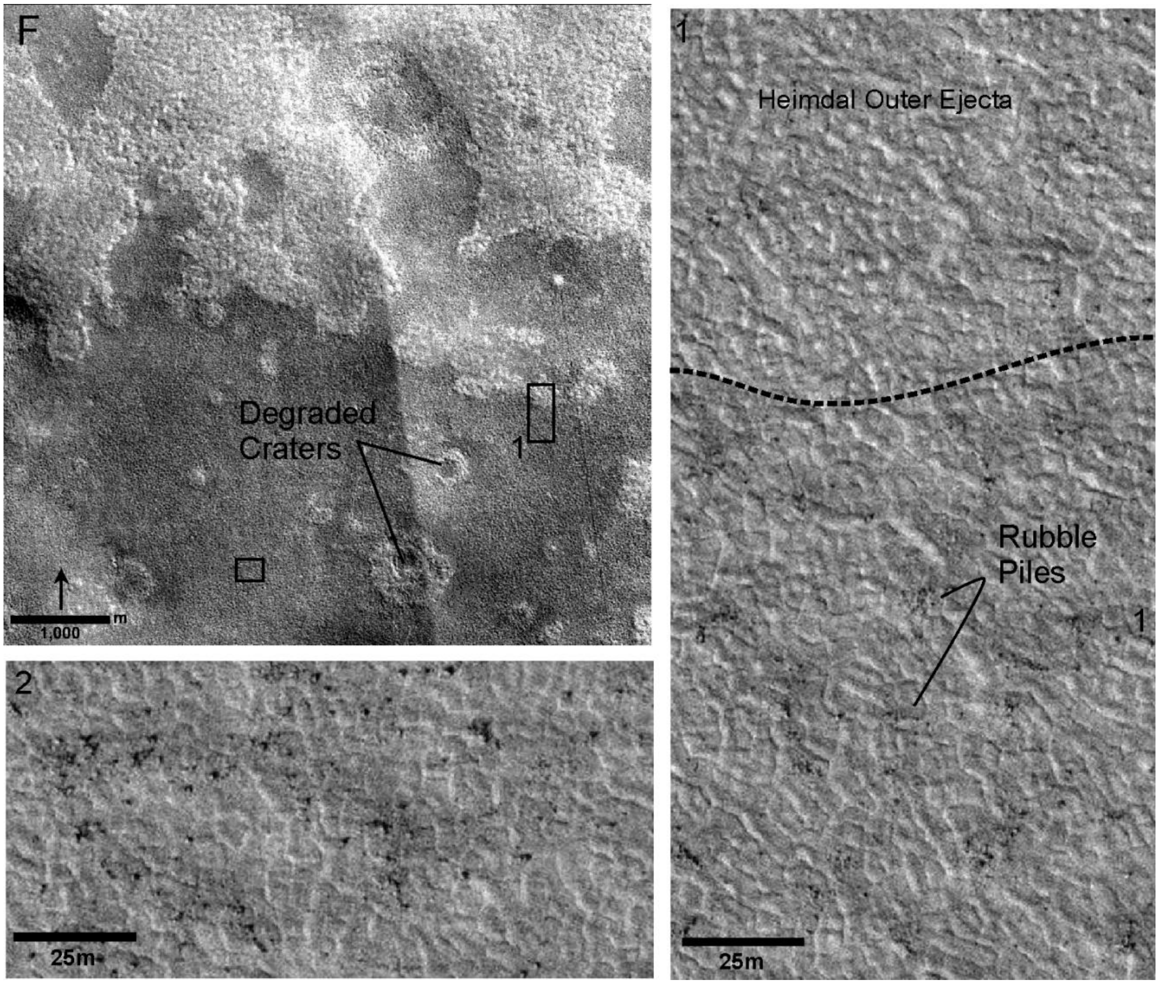

Figure 9. Portion of CTX image P02_001959_2484_XI_68N127W showing the boundary zone between Heimdal Outer Ejecta and Lowland Plains. Numerous degraded, sometimes pedestal type, craters are visible on both units in this area. In CTX these units are differentiated mainly by albedo. (1) In HiRISE (PSP_001959_2484) the two units can be differentiated by rock abundance, (2) rocks being much more abundant in the Lowland Plains and present as rubble piles spaced on average 20m apart. The albedo differences are due to a 2-3% greater rock shadow coverage in the Lowland Plains.

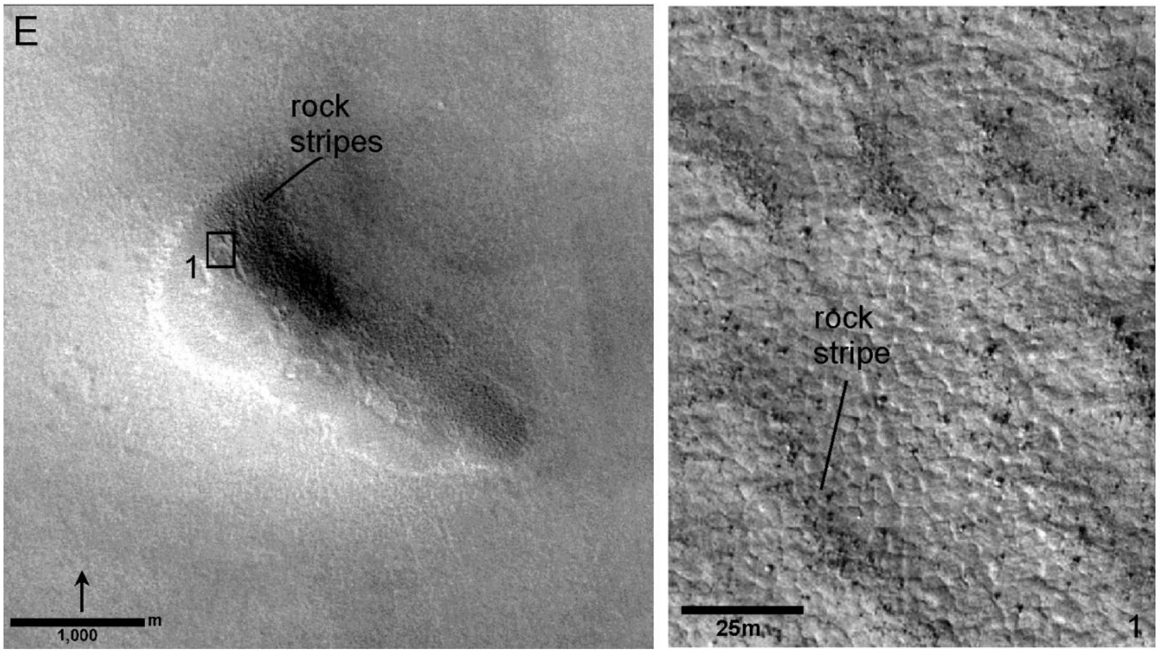

Figure 10. Portion of CTX image P02_001983_2485_CI_68N126W showing an example of Knobby Terrain. This hill is located ~50km from Hiemdal crater rim and rises ~50m above the surrounding Heimdal Outer Ejecta. It is most likely a pre-existing landform with too much topographic relief to be eradicated by the impact. (1) Rocks were also protected from eradication and exist as linear features. Note also the ubiquitous ~5m scale patterned ground.

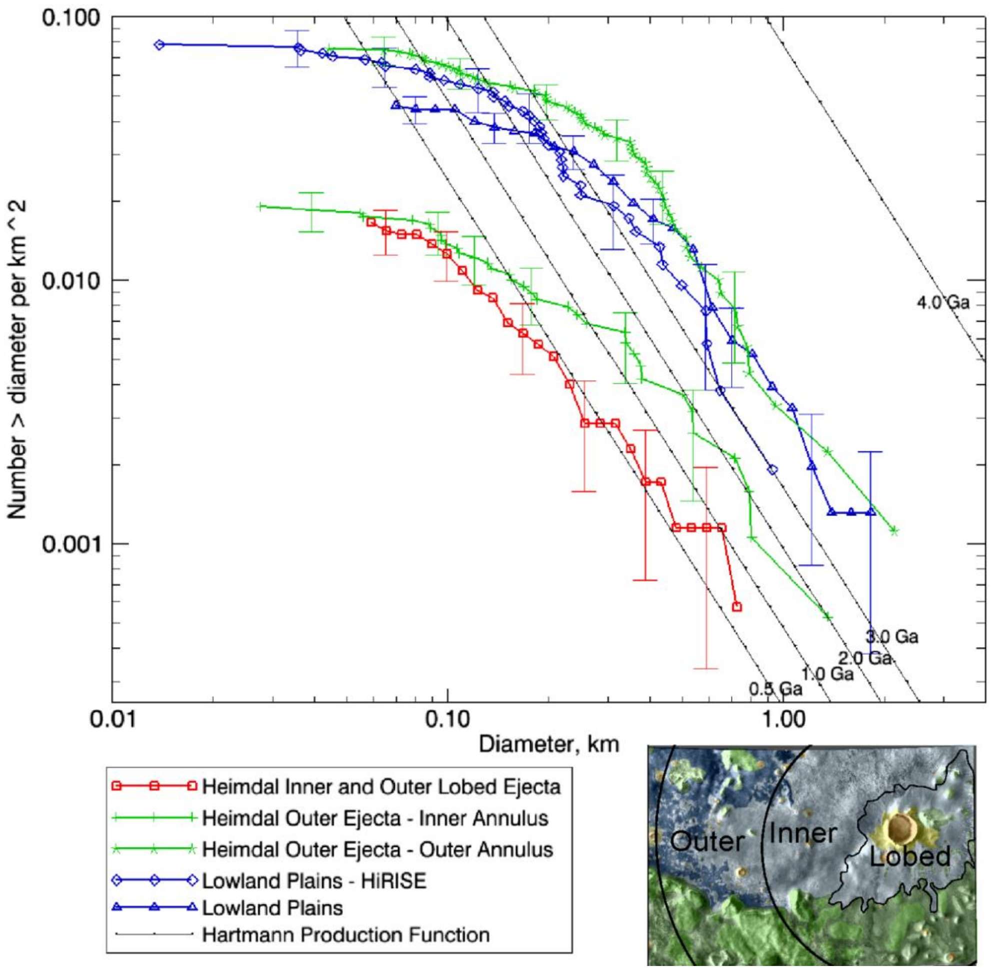

Figure 11. Observed crater size-frequency distributions for the Heimdal Outer Ejecta and Heimdal Inner and lobed portion of Outer Ejecta. Solid black lines are Hartmann production functions for 0.5 (bottom curve), 1.0, 2.0, 3.0, and 4.0 Ga. Heimdal Inner and Outer lobed Ejecta is ~600 million years old. The Lowland Plains date to ~3.3Ga which corresponds to the beginning of the Amazonian period of mars history [Hartmann and Neukum 2008]. Crater counts for the Heimdal Outer Ejecta, excluding the lobed deposits, were divided into inner and outer facies. The inner counts are similar to Hiemdal Inner Ejecta, while the outer counts are equivalent to the Lowland Plains, indicating that there is a gradient in crater abundance, increasing far from Heimdal. The Outer Ejecta represent a differentially modified surface in terms of landforms associated with the Heimdal impact. Note also the deviation from Hartmann

production functions for each unit starting at a crater size of ~300m. After visual inspection of craters in HiRISE, notional modeling of crater distributions, and explicit treatment of contrast reduction due to haze, we hypothesized this decrease in slope is indicative of a depth dependent removal of craters, with small sizes removed faster than larger.

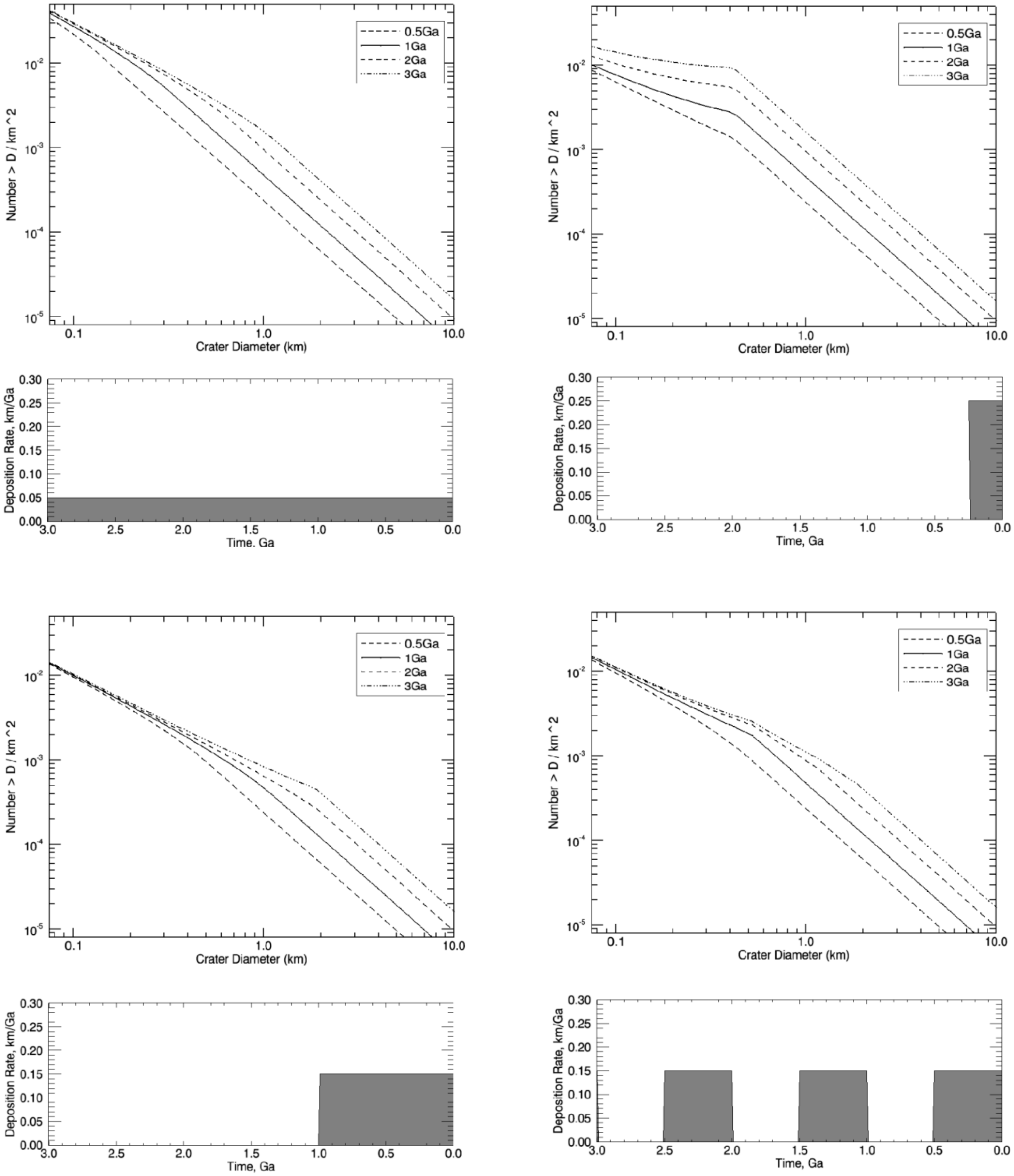

Figure 12. (a) Modeled crater size-frequency distributions for a constant deposition of 0.5 km/Ga and starting at the time of formation of the oldest surface. Shown for surface formation times of 1, 2, and 3Ga. Change in slope occurs at larger diameters for older surfaces. At small

diameters the curves converge. (b) Modeled crater size-frequency distributions for deposition beginning at 0.25Ga at a rate of 0.25 km/Ga and continuing to present. Shown for surface formation times of 1, 2, and 3 Ga. Change in slope occurs at the same crater diameter regardless of age. Curves do not converge at small diameters. Also note that a more extreme change in slope can be obtained than in (a). (c) Modeled crater size-frequency distributions for deposition beginning at 1Ga at a rate of 0.15km/Ga and continuing to present. Shown for surface formation times 1, 2, and 3Ga. Change in slope occurs at similar sizes for older surfaces, but for the 1Ga old surface the change in slope is more subdued and occurs at a smaller diameter. (d) Model crater size-frequency distribution for discrete periods of deposition at a rate of 0.15km/Ga. Older surfaces are characterized by multiple changes in slope. Model (b) most closely models the change in slope at ~300m observed at the landing site.

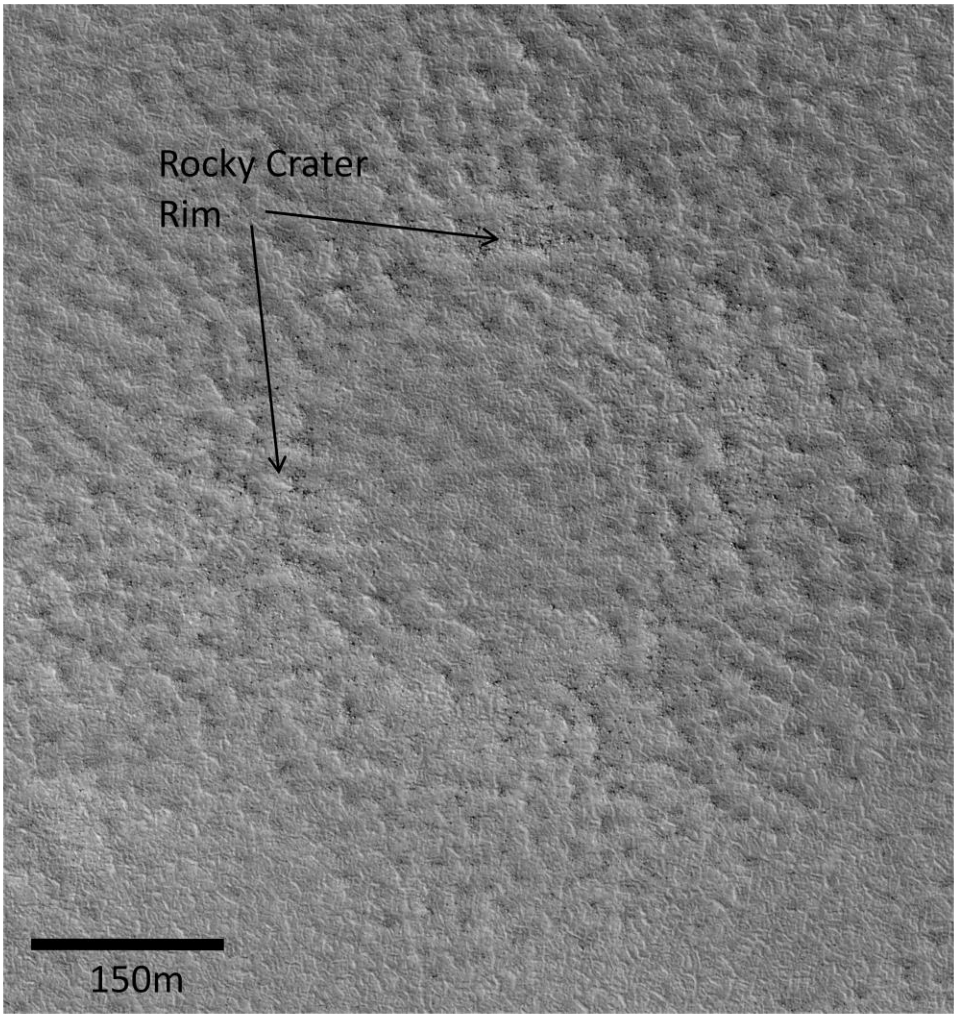

Figure 13. Portion of HiRISE image PSP-002012_2485 showing a severely degraded crater with a preserved rocky rim within the Lowland Plains. The rocky rim and ejecta suggests that infill cannot be the only process degrading craters as the rocks would also be covered during this process. Other mechanisms could include viscous relaxation of a shallow ice table and cryoturbation.

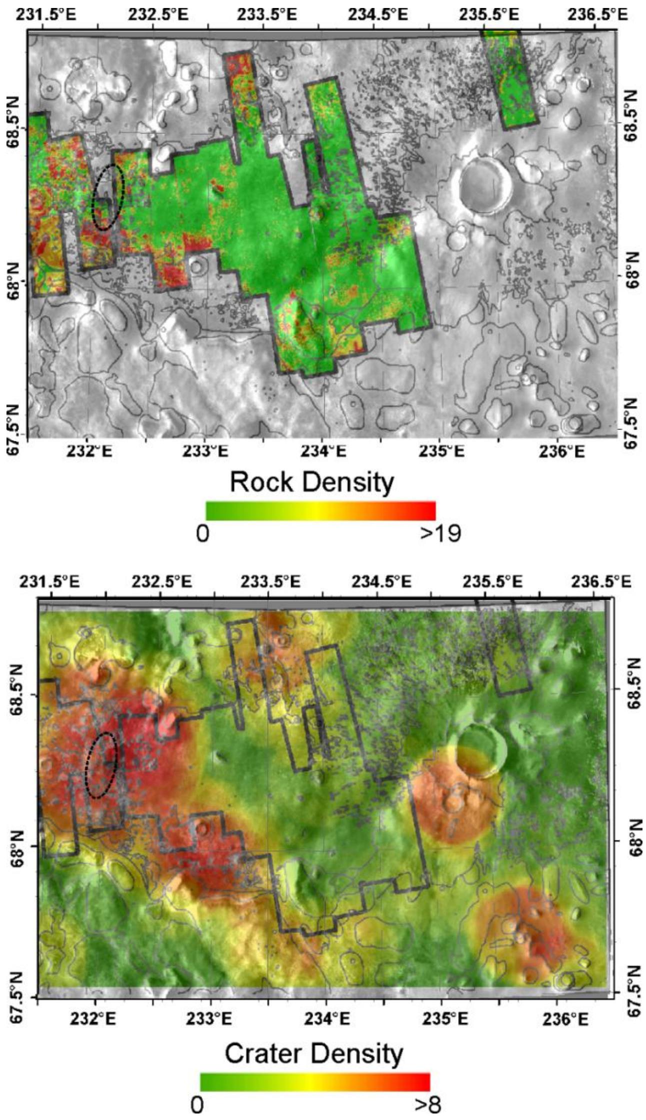

Figure 14. (a) Polar Stereographic map showing rock density. Background is a THEMIS visible mosaic. Green = 0-3, Yellow = 4-9, Orange = 9-19, and Red = >19 rocks larger than 1.5 meters per hectare. Pixel size is 1 hectare. Gray lines indicate outlines of geologic units. (b) A Polar Stereographic map of crater density, on a THEMIS visible mosaic background, shows that rocks and craters visually correlate spatially. Color scale represents the number of overlapping crater regions, where crater region in this context is defined as the circular region extending for a distance equal to 5 radii beyond the crater rim. The black outline shows the area over which rock density was calculated. (c)

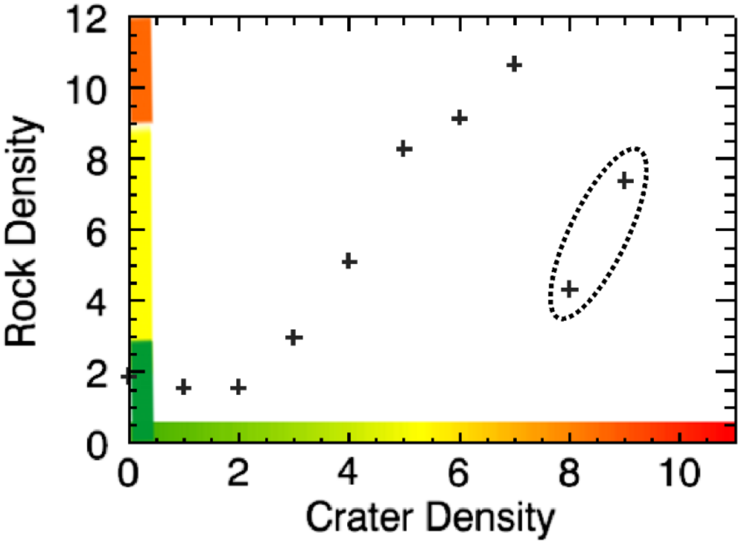

Figure 15. The average rock density corresponding to each crater density value in Figure 15 was derived by pixel-to-pixel comparison of the density maps. In general rock and crater density are positively correlated. This correlation breaks down at crater densities of around 8. On the maps this correlates to the Lowland Plains/Heimdal Outer Ejecta boundary. This correlation also does not work in the case of Heimdal, which is characterized by the lowest rock abundance in the region. Both of these discrepancies are best explained as an effect of vapor-charged ground hugging flow that removed rocks and landforms during Heimdal ejecta emplacement, with obliteration capability greater close to the impact.

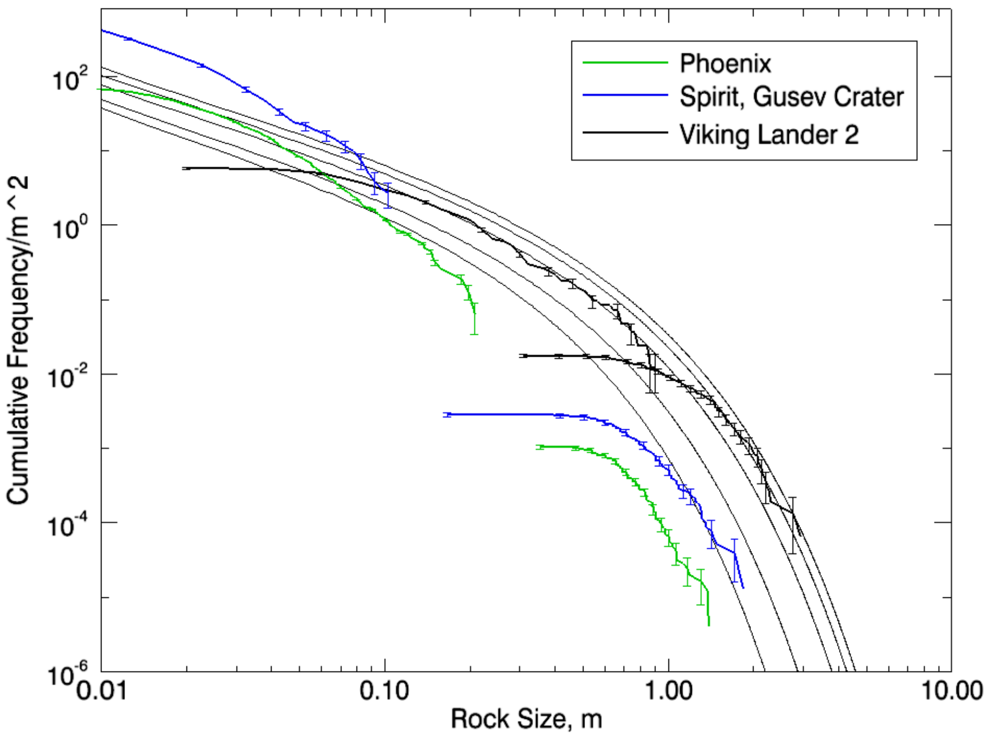

Figure 16. Rock cumulative size-frequency distributions derived from HiRISE and surface data for Phoenix, VL2 and Spirit landing sites. Solid black lines are models for rocks covering 5 (lowest curve), 10, 20, 30, and 40% of the surface. The Phoenix site is depleted in rocks of all sized relative to the Spirit Rover and Viking sites. Both Phoenix and Spirit sites exhibit a steeper slope than predicted by models , a trend seen also at the Mars Pathfinder site and several earth analogue sites (Golombek and Rapp 1997). This deviation from the model suggests that similar processes are in operation at the Phoenix and Spirit sites, which differ from processes in action at the VL2 site. Note that the flattening of distribution curves at small rock sizes is a result of the resolution limit of the images used to derive the distributions.

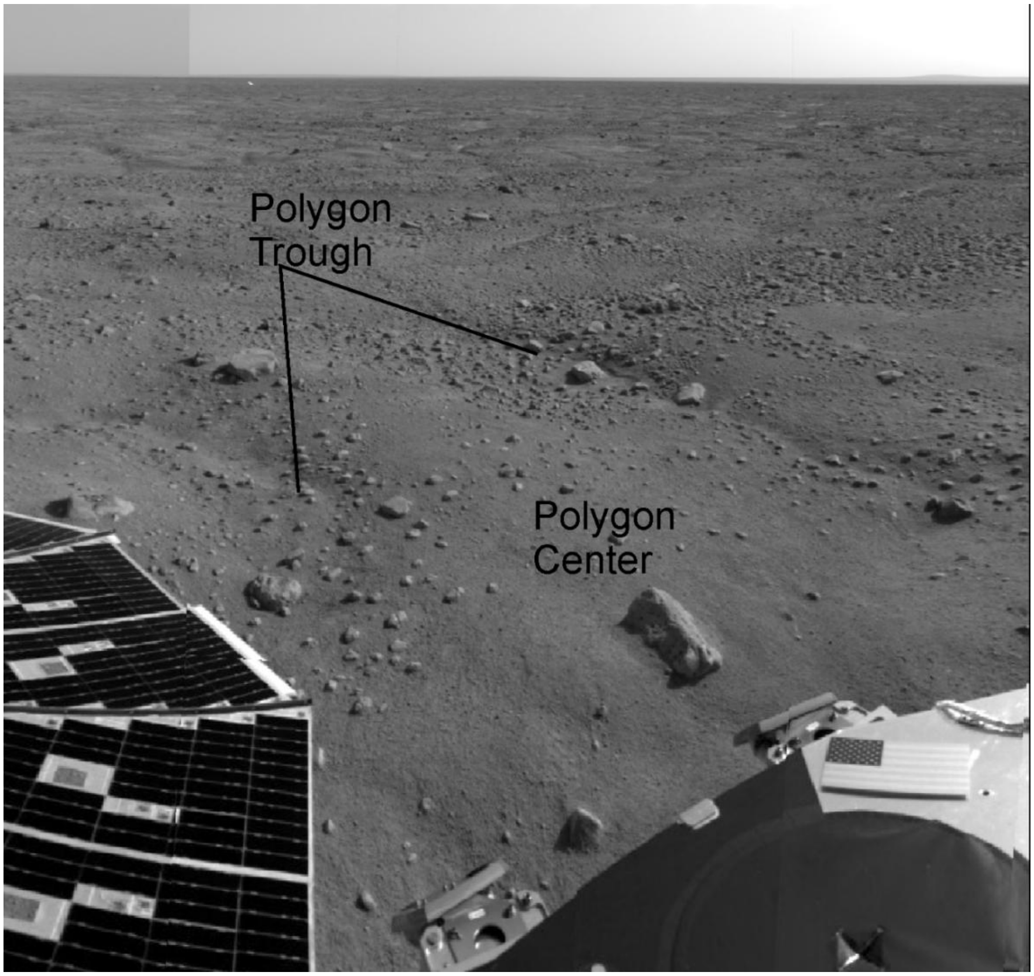

Figure 17. SSI mosaic of a portion of the Phoenix landing site (cylindrical projection). Rocks are visually more abundant in polygon troughs (i.e. the topographic lows in the scene).

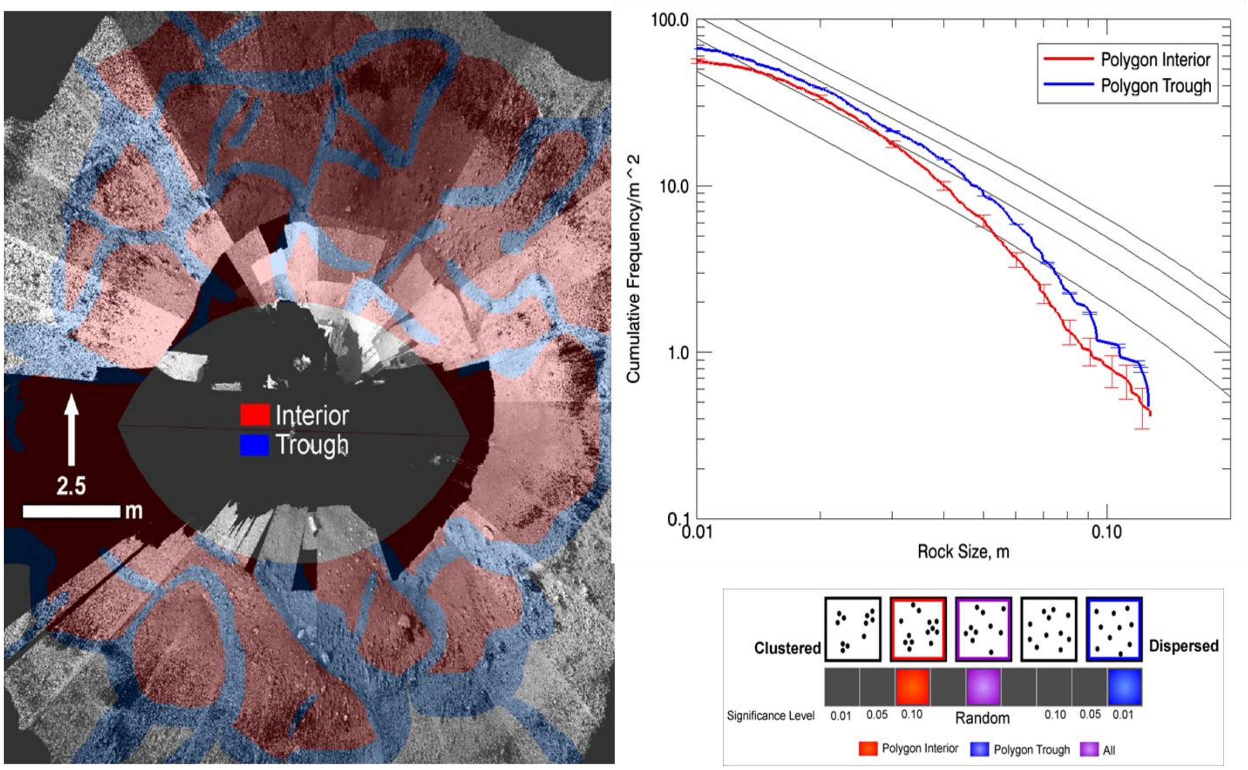

Figure 18. (left) SSI mosaic of the Phoenix landing site, projected into a Cartesian coordinate system (view looking down on lander from above). Mapped polygon interior (red) and polygon trough (blue) units are shown. Black patches far from the center of the image indicate areas where no digital elevation model information was available. Because of these holes in the data, rock distributions where characterized only within ~5 meters of the lander. (left, top) Rock cumulative size-frequency distributions derived from Phoenix SSI images. Solid black lines are models for rocks covering 5, 10, 20, 30, and 40% cumulative fractional area of the surface. Surface rock counts covering 41 square meters around the lander were divided into polygon trough and polygon interior units in order to investigate the process of polygon formation. There is a slight trend toward concentrating rocks in and chi-squared goodness-of-fit tests indicate that the two distributions are different to the 1.2e-5 significance level. Rock sorting into polygon troughs would be expected if thermal contraction based polygon formation was active. (left, bottom) Schematic representation of the nearest neighbor statistic. Rocks within polygon

interiors tend to be clustered, whereas rocks within polygon troughs tend to be uniformly dispersed. When the landing site is analyzed as a whole rocks are best described as a random distribution. The significance level represents the likelihood that the observed pattern is the result of random chance.

Tables

Table 1. Relevant CTX and HiRISE image information

CTX Image File name	Ls	Incidence angle	emission angle	phase angle	center lat	center lon
P17_007866_2481_XI_68N124W	52.41	53.38	11.83	63.38	68.11	124.36
P16_007128_2484_XI_68N128W	26.5	61.82	5.91	57.61	68.42	128.46
P03_002183_2492_XI_69N123W	166.1	70.46	2.58	72.75	69.28	123.73
P04_002539_2490_XI_69N124W	181.44	76.27	9.36	84.4	69	124.37
P15_007062_2483_XI_68N126W	24.11	62.53	4.31	59.5	68.41	126.8
P15_006996_2481_XI_68N126W	21.71	62.83	2.12	64.42	68.14	126.12
P15_006851_2482_XN_68N125W	16.38	65.12	3.78	62.58	68.29	125.84
P04_002526_2482_XI_68N125W	180.86	76.53	4.46	72.74	68.27	125.89
P03_002249_2483_XI_68N125W	168.89	71	4.53	75	68.34	125.62
P14_006706_2484_XI_68N126W	10.97	67.25	3.92	64.7	68.48	126.83
P04_002447_2483_XI_68N128W	177.4	75.39	7.66	68.83	68.41	128.44
P03_002381_2482_XI_68N128W	174.54	73.71	1.5	72.46	68.28	127.95
P04_002605_2488_XI_68N125W	77.6	5.9	82.72	68.81	125.37	
P03_002328_2485_XI_68N125W	172.26	71.64	18.07	87.49	68.59	125.8
P03_002315_2487_XI_68N126W	171.7	72.65	0.19	72.83	68.72	126.66
P03_002104_2485_XI_68N126W	162.79	68.83	0.62	69.42	68.54	126.13
P15_006785_2482_XN_68N125W	13.93	65.69	2.87	67.74	68.28	125.3
P15_006930_2478_XN_67N123W	19.3	63.64	1.25	62.82	67.86	123.21
P02_002012_2485_XI_68N128W	158.99	68.97	22.75	49.59	68.55	128.79
P02_001972_2485_XI_68N128W	157.35	65.07	24.16	86.56	68.62	128.19
P15_007009_2495_XN_69N121W	22.19	63.77	0.1	63.84	69.51	121.18
P17_007853_2483_XI_68N125W	51.96	54.61	4.86	50.71	68.32	125.65
P02_001906_2484_XI_68N126W	154.66	63.88	24.86	86.04	68.49	126.39
P01_001418_2494_XI_69N125W	135.51	59.16	0.09	59.21	69.47	125.79
P02_001761_2493_XN_69N122W	148.84	63.75	0.08	63.8	69.33	122.51
P02_001880_2484_XI_68N128W	153.61	65.86	10.36	56.88	68.47	128.04
P02_001946_2484_XI_68N127W	156.29	67.62	19.64	50.8	68.51	127.7
P02_001893_2485_XI_68N126W	154.14	64.96	6.5	70.75	68.54	126.88
P15_007075_2484_XI_68N124W	24.59	61.71	9.05	68.48	68.43	124.81
P18_008143_2483_XI_68N125W	61.89	52.49	1.22	51.51	68.34	125.19
P02_001959_2484_XI_68N127W	156.82	66.36	0.65	66.97	68.43	127.39
P17_007708_2484_XI_68N126W	46.96	55.94	6.48	50.84	68.42	125.93
P17_007721_2487_XI_68N122W	47.41	55.62	0.09	55.68	68.72	122.51
P17_007774_2486_XI_68N128W	49.24	55.44	5.34	51.21	68.62	128.48

P17_007787_2481_XI_68N125W	49.69	54.6	1.87	56.19	68.13	124.89
P18_007919_2484_XI_68N126W	54.23	54.52	10.11	46.4	68.42	126.68
P18_007998_2484_XI_68N125W	56.93	53.54	3.09	51.03	68.43	125.47
P18_008064_2483_XI_68N127W	59.19	53.24	6.02	48.28	68.31	126.94
P18_008077_2482_XI_68N124W	59.63	52.47	4.03	55.95	68.2	124.14
P18_008130_2484_XI_68N127W	61.44	53.41	13.54	42.36	68.41	127.4
P22_009580_080811	111.43	52.43	4.88	56.86	68.55	124.5
P22_009725_2484_XI_68N125W	116.64	52.67	15.59	66.91	68.39	125.68
HiRISE Image File name						
PSP_001418_2495_RED	135.505	59.0132	0.23754	59.1408	69.2435	234.301
PSP_001761_2495_RED	148.841	63.6069	0.22993	63.7336	69.1239	237.66
PSP_001880_2485_RED	153.608	65.7167	10.3748	56.7957	68.2596	232.164
PSP_001893_2485_RED	154.133	64.8089	6.52483	70.6852	68.4623	233.34
PSP_001906_2485_RED	154.66	63.6922	24.9123	85.976	68.4113	233.863
PSP_001946_2485_RED	156.285	67.4997	19.6649	50.7185	68.4242	232.549
PSP_001959_2485_RED	156.815	66.1975	0.69641	66.8876	68.3506	232.852
PSP_001972_2485_RED	157.346	64.8769	24.2135	86.4843	68.4711	232.037
PSP_002012_2485_RED	158.985	68.8562	22.7856	49.5056	68.3797	231.45
PSP_002025_2485_RED	159.52	67.3306	0.2474	67.467	68.3054	231.066
PSP_002091_2485_RED	162.249	69.5367	15.5369	56.2467	68.199	232.792
PSP_002104_2485_RED	162.789	68.6854	0.67255	69.3525	68.4823	234.096
PSP_002170_2485_RED	165.548	70.0556	3.14524	67.4395	68.4207	233.075
PSP_002183_2495_RED	166.094	70.3246	2.59665	72.6882	69.1126	236.425
PSP_002249_2485_RED	168.882	70.8974	4.54508	74.9608	68.2666	234.503
PSP_006640_2485_RED	8.4707	67.6253	0.25745	67.8294	68.1426	234.639
PSP_006706_2485_RED	10.9629	67.0419	3.91902	64.603	68.3836	233.398
PSP_006785_2485_RED	13.9219	65.4779	2.90337	67.6563	68.2211	234.927
PSP_006851_2480_RED	16.3748	64.8917	3.77173	62.4673	68.1363	234.39
PSP_006930_2480_RED	19.2887	63.4625	1.2604	62.761	67.7964	236.995
PSP_006996_2480_RED	21.7056	62.6939	2.14941	64.4027	68.2476	234.103
PSP_007062_2485_RED	24.1071	62.3846	4.30468	59.4661	68.3846	233.395
PSP_007128_2485_RED	26.4941	61.8024	5.90839	57.7012	68.5544	231.676
PSP_007141_2485_RED	26.9626	60.7509	8.30629	67.1336	68.4107	233.588
PSP_007497_2480_RED	39.6049	56.9802	2.89921	59.4095	68.1454	233.91
PSP_007629_2485_RED	44.2134	56.5993	6.13453	51.9315	68.6511	231.337
PSP_007642_2480_RED	44.6653	55.5224	4.25449	59.101	68.1667	234.217
PSP_007708_2485_RED	46.9549	55.7064	6.48268	50.6946	68.3145	234.365
PSP_007721_2480_RED	47.4049	54.858	0.2501	55.0185	67.7746	238.148
PSP_007774_2485_RED	49.2369	55.2823	5.33739	51.1395	68.6508	231.78
PSP_007787_2480_RED	49.6855	54.4931	1.9043	56.1821	68.2513	235.319

PSP_007853_2485_RED	51.9593	54.4426	4.86163	50.6253	68.3226	234.611
PSP_007866_2480_RED	52.4064	53.2172	11.868	63.3313	68.0889	235.854
PSP_007919_2485_RED	54.227	54.3678	10.1125	46.319	68.4348	233.581
PSP_007932_2480_RED	54.673	53.2726	3.53231	56.3571	68.2235	235.613
PSP_008064_2485_RED	59.1914	53.1142	6.02262	48.2394	68.374	233.303
PSP_009290_2485_RED	101.189	51.1067	0.51871	50.8058	68.3724	234.469
PSP_002315_2485_RED	171.695	72.5521	0.22202	72.7725	68.7674	233.54
PSP_002328_2485_RED	172.252	71.5039	18.1036	87.415	68.6825	234.439
PSP_002381_2485_RED	174.533	73.5663	1.50778	72.3965	68.1513	232.243
PSP_002447_2485_RED	177.397	75.2285	7.67019	68.7446	68.2999	231.798
PSP_002526_2485_RED	180.857	76.3984	4.46364	72.6845	68.3175	234.355
PSP_002539_2490_RED	181.43	76.1174	9.38799	84.3454	69.052	235.906
PSP_007352_2480_RED	34.4967	58.5365	1.64949	59.9508	68.1192	233.626
PSP_009079_2485_RED	93.8568	50.6097	1.55758	49.3487	68.4985	235.412
PSP_009092_2485_RED	94.3062	49.1667	19.3835	66.8808	68.514	235.483

Table 2. Crater Count Parameters

Geologic Unit	Age (Ga)	Deposition Rate (km/Ga)						
		0.0-1.0	1.0-2.0	2.0-3.0	3.0-3.5	3.5-3.99	4.0-4.25	4.25-4.5
Heimdal Inner and lobed Ejecta	0.6	-	-	-	-	-	0.001	0.15
Heimdal Outer Ejecta	3.1	-	0	0	0	0.02	0.07	0.08
Lowland Plains	3.3	-	0.05	0	0	0.03	0.00001	0.12
Highland Plains	3.4	-	0	.19	0.01	0.003	0.1	0.13
Blocks and Mesas	3.5	-	0	0	0	0	0	0

Table 3. Summary of Nearest Neighbor Statistics

Unit	**Area, m^2**	**Observed mean distance/expected mean distance**	**z-score**	**Significance level**	**Description**
Polygon Combined	41.4	0.98	-0.54	-	Random
Polygon Interior	28.6	0.93	-1.74	0.1	Clustered
Polygon Trough	12.8	1.25	5.04	0.01	Uniform/dispersed

Appendix A. Data Set Specifications

Here we review the specifications of orbital - CTX, HiRISE, CRISM, THEMIS, and MOLA -and Phoenix - SSI - data sets used in this study. A section explaining the cartographic methodology is also given. Standard Data Products for each data type are archived and publicly available through the NASA Planetary Data System (PDS).

CTX: The Context Camera (CTX) instrument onboard the Mars Reconnaissance Orbiter (MRO) has been in operation in a nearly circular, nearly polar mapping orbit since March 2006 [*Malin et al.* 2007]. Images used in this study were acquired between November 2006 and September 2008. CTX acquires ~30km wide images with one band pass of 500-700nm and a spatial resolution of 5-6m [*Malin et al.* 2007].

The CTX images used in this study have been geometrically calibrated, map-projected, and contrast stretched by the CTX team at Malin Space Science Systems. The map-projected images were imported into ENVI and mosaicked together to form a single base map at 5.0001 m/pixel spatial resolution. Due to variability of atmospheric haze over the landing site, some images resolved smaller features than others. Care was taken to ensure that the sharper images were placed above hazy images in the mosaic. The complete list of CTX images comprising the mosaic are presented in Table 1.

HiRISE: The High Resolution Imaging Science Experiment (HiRISE) on board Mars Reconnaissance Orbiter has been in operation since March 2006 [*McEwen et al.* 2007]. Images used in this study were acquired between September 2006 and July 2008. A comprehensive list of images used is provided in Table 1. HiRISE acquires ~6km wide images at 25.5-32 cm/pixel spatial resolution with three band passes (RED: 570-830 nm, BG: <580nm, and NIR: >790nm) [*McEwen et al.* 2007].

The HiRISE images used in this study have been radiiometrically corrected and geometrically transformed to standard Polar Stereographic map projections in Planetocentric coordinates at 0 degrees center longitude by the MRO HiRISE team [*McEwen et al.* 2007]. In general, we used images acquired from the RED band pass (570-830 nm) though some color images were also utilized. Because of their large size (~1.5Gb) only small portions of these images were re-projected to North Polar Stereographic with center longitude 126.5W to match the CTX base map and none were mosaicked. To locate images of interest we imported HiRISE footprints as a vector layer into ArcGIS ArcMap along with the CTX base map. We could then locate the appropriate HiRISE image and view the image in either ArcMap or ENVI when it was of interest, without having to deal with a very large mosaic of HiRISE images. Images used in rock counts were individually examined and subset as they were acquired as part of pre-landing landing site hazard assessments.

CRISM : The Compact Reconnaissance Imaging Spectrometer for Mars (CRISM) is a hyperspectral imager on the MRO spacecraft. CRISM operates in three different modes. In multispectral mapping model data are collected at a subset of 72 wavelengths covering key mineralogical absorptions and binned to pixel footprints of 100 or 200 m/pixel [*Murchie et al.* 2007]. Nearly the entire planet can be mapped in this fashion [*Murchie et al.* 2007]. In targeted mode the region of interest is mapped at full spatial and spectral resolution (15-19 m/pixel, 362-3920nm at 6.55 nm/channel) [*Murchie. et al.* 2007]. Ten additional abbreviated spatially binned images are taken before and after the main image, providing an emission phase function (EPF) for atmospheric study and correction of surface spectra for atmospheric effects [*Murchie et al.* 2007]. In atmospheric mode, only the EPF is acquired.

For this study we used a single CRISM image acquired in Full Resolution Targeted mode, FRT0003957 covering the boundary between Heimdal Outer Ejecta and the Lowland Plains. The image was processed to Spectral Lambert Albedos for each pixel using DISORT-based retrieval in which dust and ice aerosols, combined with gas bands were explicitly modeled using techniques presented in *Arvidson et al.* [2006].

THEMIS: The Thermal Emission Imaging System (THEMIS) is a multispectral camera with five wavelengths in the visible (0.425 – 0.860 µm) and ten in the infrared (6.78-14.88 µm) [*Christensen et al.*2004] . THEMIS acquires data in the visible region at 18 m/pixel and in the infrared at 100 m/pixel spatial resolution [*Christensen et al.*2004]. THEMIS images used in this study have been geometrically and radiometrically calibrated, map-projected, contrast stretched, and mosaicked together by the THEMSI science team at Arizona State University as part of their participation in the Phoenix Mission. Daytime and nighttime infrared mosaics have pixel values maintained to reflect geophysical units. A visible map-projected mosaic was also created with any gaps filled in using daytime infrared images resampled to 18 m/pixel.

MOLA : The Mars Global Surveyor (MGS) Mars Orbiter Laser Altimeter (MOLA) is a laser ranging device used to acquire global topography of the Martian surface [*Zuber et al.* 1992]. It derives elevation by measuring the round trip time of flight of infrared laser pulses (1064 nm) transmitted from the MGS spacecraft to the Martian surface [*Zuber et al.* 1992]. Individual shots have on average a ~130 m footprint (size decreases near the poles) and are spaced ~300m apart. Because each shot has a high signal to noise ratio only one shot is needed to accurately determine altimetry at that point. The resulting dense network of shots from multiple tracks over its 4 year operating period allowed gridded topographic images to be produced at 100 m/pixel spatial resolution over the landing site and with elevations reported relative to the MOLA defined aeroid [*Zuber et al.* 1992].

The MOLA image used in this study was downloaded from the PDS as part of the global gridded product, subset to cover the study area, and re-projected from a North Polar Stereographic projection with center longitude 0, to a North Polar Stereographic projection with center longitude 126.5W. Color products were produced in both ENVI and ArcMap to better visualize topography.

SSI: The Surface Stereo Imager (SSI) is a panoramic camera on the Phoenix lander. It acquires images from a 2m high mast overlooking the digging area. With two cameras separated by ~15cm it is capable of simulating human vision as well as providing a digital elevation model of the local surface. It consists of 13 filters that span the spectral range from 440 to 1000nm.

For this study we used radiometrically calibrated linearized reduced data records and associated digital elevation model to create a cartesian coordinate mosaic of the landing site extending out to a 10m radius around the lander. The pixel size was set to 1mm, though in the original images the pixel size was not constant. Holes of missing data are present within the final mosaic because the SSI could not see behind certain obstacles such as rocks and dump piles. The SSI mosaic was used to map polygons and count and measure rocks.

Cartographic Methodology: The CTX, THEMIS and MOLA data sets were all imported into a GIS environment and converted to a North Polar Stereographic projection with center longitude 233.5E. Select HiRISE and CRISM images were also imported as separate layers. Mapping was accomplished by tracing unit contacts as a set of polygon-type feature classes in ArcMap.

Crater counts were done using the CTX mosaic and tracing crater rims in ArcMap. Crater diameters were calculated based on the perimeter length. Crater counts for individual units were derived by cropping the original crater outlines by the unit of interest.

Orbital rock counts were done using HiRISE and measuring the shadow width perpendicular to the sun azimuth for selected areas within each HiRISE image. These hand counts were used to calibrate the auto-counting method used to determine rock abundances for the majority of the landing site. Surface rock counts were determined using the SSI mosaic and measuring the short and long dimensions of each rock within a 5m radius of the lander. Rock size was defined as the average of the two. Nearest neighbor statistics were calculated using the Average Nearest Neighbor tool in the Spatial Statistics toolbox.

Polygons units were defined based on elevation. The Polygon Interior corresponds to the raised central portion of the polygon and the Polygon Trough unit corresponds to the depressed edges. The boundary between the two units was defined as the halfway point in elevation between the highest portion of the Polygon Interior and the bottom of the trough. A combination of colorized digital elevation models and 1cm contours were used to determine elevation. Mapping was done by tracing the contact between units in ArcMap as a polygon-type feature class.